Research Square

Preprints are preliminary reports that have not undergone peer review.
They should not be considered conclusive, used to inform clinical practice,
or referenced by the media as validated information.

Super-Enhancer-Driven ZMYND8 Sustains Neuroblastoma Growth via a CDK6-Associated Transcriptional Program

Yan-Fang Tao

taoyanfang19820163.com

Children's Hospital of Soochow University

Di Wu

Children's Hospital of Soochow University

Chun Yang

Soochow University Affiliated Children's Hospital

Li Xia

Children's Hospital of Soochow University

Yanling Chen

Children's Hospital of Soochow University

Ran Zhuo

Children's Hospital of Soochow University

Gen Li

Children's Hospital of Soochow University https://orcid.org/0000-0003-0087-7796

Xiao-Lu Li

Children's Hospital of Soochow University

Yang Yang

Children's Hospital of Soochow University

Juan-Juan Yu

Children's Hospital of Soochow University

Jia Cheng

Children's Hospital of Soochow University

Xue Li

Children's Hospital of Soochow University

Chunxia Shi

Children's Hospital of Soochow University

Tong Liu

Children's Hospital of Soochow University

LANLAN HAN

Suzhou Medical College of Soochow University
Jiasi Liu
Children's Hospital of Soochow University
Jian Pan
Children's Hospital of Soochow University https://orcid.org/0000-0002-0292-5141
Zimu Zhang
Children's Hospital of Soochow University https://orcid.org/0000-0002-7791-4252

Article

Keywords: neuroblastoma, super-enhancer, ZMYND8, CDK6, HMN-176

Posted Date: September 18th, 2026

DOI: https://doi.org/10.21203/rs.3.rs-10955590/v1

License: This work is licensed under a Creative Commons Attribution 4.0 International License.
Read Full License

Additional Declarations: (Not answered)

Super-Enhancer-Driven ZMYND8 Sustains Neuroblastoma Growth via a CDK6-Associated Transcriptional Program

Di Wu[1#], Chun Yang[1#], Li Xia[1#], Yanling Chen[2#], Ran Zhuo[3#], Gen Li[1], Xiaolu Li[1], Yang Yang[1], Juanjuan Yu[4], Jia Cheng[1], Xue Li[1], Chunxia Shi[1], Tong Liu[1], Lanlan Han[1], Jiasi Liu[1], Jian Pan[1*], Zimu Zhang[1*], Yanfang Tao[1,5*]

1. Institute of Pediatric Research, Children's Hospital of Soochow University, Suzhou, Jiangsu, 215003, China.

2. Department of Hematology, Affiliated Children's Hospital of Jiangnan University (Wuxi Children's Hospital), Wuxi, Jiangsu, 214023, China.

3. Department of Pediatric Surgery, Children's Hospital of Soochow University, Suzhou, Jiangsu 215025, China.

4. Department of General Surgery, Children's Hospital of Soochow University, Suzhou, Jiangsu, 215003, China.

5. Department of Traditional Chinese Medicine, Children's Hospital of Soochow University, Suzhou, Jiangsu, 215003, China.

[#] These authors contributed equally to this work

***Corresponding author:**

Yanfang Tao, Institute of Pediatric Research, Children's Hospital of Soochow University; Department of Traditional Chinese Medicine, Children's Hospital of Soochow University, No.92 Zhongnan Street, SIP, Suzhou, Jiangsu, 215003, China. Tel: 86-0512-80691508; E-mail: taoyanfang1982@163.com

***Corresponding author:**

Zimu Zhang, Institute of Pediatric Research, Children's Hospital of Soochow University, No.92 Zhongnan Street, SIP, Suzhou, Jiangsu, 215003, China. Tel: 86-0512-80692935; E-mail: mumuhere@qq.com

***Corresponding author:**

Jian Pan, Institute of Pediatric Research, Children's Hospital of Soochow University, No.92 Zhongnan Street, SIP, Suzhou, China, 215003. Tel: 86-0512-80692935; E-mail: panjian2008@163.com

Abstract

Neuroblastoma (NB) exhibits pronounced transcriptional heterogeneity, driven largely by super-enhancers (SEs), yet the downstream effectors of SEs remain incompletely characterized. Here, we systematically investigated the SE-dependent regulation, biological function, and therapeutic potential of ZMYND8 in NB by integrating H3K27ac ChIP-seq, Hi-C/Capture Hi-C, CRISPR/Cas9-mediated enhancer disruption, multi-omics profiling, and structure-based virtual screening. We found that ZMYND8 is regulated by a BRD4-dependent SE across multiple NB cell lines, with the enhancer element E1 serving as a core regulatory component essential for ZMYND8 transcription and NB cell proliferation. Genetic depletion of ZMYND8 significantly impaired proliferation and colony formation, induced apoptosis, and suppressed tumor growth in xenograft models. Integrated RNA-seq, ATAC-seq, and CUT&Tag analyses revealed that ZMYND8 sustains the E2F and G2/M transcriptional programs, identifying CDK6 as a critical downstream effector. Structure-based virtual screening identified HMN-176 as a lead compound that reduced ZMYND8 protein and CDK6 expression, triggered apoptosis, and inhibited tumor growth in both human NB xenograft and murine NB models, without evident toxicity. Collectively, these findings define a BRD4/SE–ZMYND8–CDK6 regulatory axis in which SE-driven ZMYND8 maintains NB growth through a CDK6-associated transcriptional program, and support ZMYND8 as a potential therapeutic vulnerability in high-risk NB.

Keywords: neuroblastoma; super-enhancer; ZMYND8; CDK6; HMN-176

1. Introduction

Neuroblastoma (NB) is among the most common extracranial solid tumors in children. It originates from neural crest–derived precursor cells of the sympathetic

nervous system and exhibits marked clinical and molecular heterogeneity[1]. Some low-risk tumors can regress spontaneously or can be successfully treated with limited therapy, whereas high-risk NB is frequently associated with extensive metastasis, therapeutic resistance and poor survival[1,2]. Several recurrent genetic alterations are strongly associated with NB pathogenesis, including MYCN amplification, activating ALK mutations, and ATRX alterations. Among them, MYCN amplification is a major feature of high-risk NB. MYCN drives tumorigenesis by enhancing cellular proliferation and enforcing an undifferentiated, stem-like state[2-4]. However, genetic aberrations alone do not fully account for the biological complexity of NB; transcriptional regulatory networks and cell-state programs also play pivotal roles. A core regulatory circuitry (CRC) comprising transcription factors—including MYCN, PHOX2B, HAND2, GATA3, ISL1, and TBX2—orchestrates the maintenance of NB lineage identity and malignant properties[5,6]. Furthermore, MYCN (and its paralog MYC) sustains oncogenic transcription through aberrant enhancer occupancy, enhancer amplification, and enhancer hijacking[7,8]. Although multimodal therapeutic strategies—including chemotherapy, hematopoietic stem cell transplantation, differentiation therapy, and anti-GD2 immunotherapy—have improved outcomes for patients with high-risk NB, effective treatment options for relapsed or refractory disease remain limited[9]. Thus, a deeper mechanistic understanding of the transcriptional programs that sustain NB growth is essential for identifying novel therapeutic targets.

Super-enhancers (SEs) are large, clustered cis-regulatory regions characterized by exceptionally high levels of H3K27ac enrichment. They drive robust transcription of cell-identity genes by recruiting transcription factors and co-activator complexes[10,11]. Relative to typical enhancers, SEs exhibit heightened sensitivity to oncogenic signaling perturbations and are indispensable for sustaining tumor-specific transcriptional programs [12]. SE profiling has yielded critical insights into neuroblastoma (NB) cellular states. Prior studies have demonstrated that lineage-determining transcription factors—including PHOX2B, HAND2, and GATA3—are under the control of SEs in NB[5,6]. Moreover, SE aberrations can directly activate oncogenes: dysregulated enhancer activity contributes to MYCN overexpression, while genetic polymorphisms within the

LMO1 SE locus are associated with increased NB susceptibility[7,8,13]. Recent investigations have increasingly focused on downstream effector genes governed by SEs. Chen et al. reported that the BRD4 inhibitor GNE-987 potently suppressed NB cell proliferation and survival by globally disrupting the SE landscape; integrated RNA-seq and ChIP-seq analyses identified FAM163A as an SE-dependent oncogene[14]. In another study, IRF2BP2 was identified as an SE-driven gene in NB. A MYCN–MEIS2–HAND2-associated SE maintains elevated IRF2BP2 expression, and IRF2BP2, in turn, cooperates with AP-1 to remodel chromatin accessibility, upregulate ALK expression, and promote NB proliferation[15]. Collectively, these findings indicate that SEs facilitate NB progression through coordinated SE–effector–oncogene regulatory networks. Our prior work demonstrated that BRD4-targeting compounds—dBET57 and GNE-987—inhibit NB proliferation, induce apoptosis and cell-cycle arrest, and modulate SE activity[14,16]. Integrated multi-omics analyses from these studies further implicated ZMYND8 as a downstream gene whose expression is regulated by BRD4-associated SE activity.

ZMYND8—also known as RACK7 or PRKCBP1—is a chromatin-associated protein harboring multiple functional domains. Its PHD, bromodomain (BRD), and PWWP domains collectively recognize specific histone post-translational modifications and broader chromatin features, thereby facilitating the targeted recruitment of ZMYND8 to distinct genomic loci[17]. Early studies identified ZMYND8 as a key regulator in the DNA damage response, where it physically associates with the NuRD complex to coordinate transcriptional repression and DNA repair at sites of damage[18]. Subsequent work revealed additional roles for ZMYND8 in P-TEFb–dependent transcriptional elongation and enhancer function[19]. Collectively, these findings demonstrate that ZMYND8 is not solely a transcriptional repressor; rather, its functional output is highly context-dependent, varying with cellular state and local chromatin environment. Although accumulating evidence links ZMYND8 to cancer-associated transcriptional programs, its precise role exhibits marked heterogeneity across different tumor types. In neuroblastoma (NB), however, ZMYND8 function remains largely uncharacterized. Given its association with super-enhancer (SE)–

related features and its downregulation upon BRD4 inhibition, we hypothesize that ZMYND8 is itself an SE-regulated gene that contributes to oncogenic transcriptional programs in NB.

In this study, we identified robust H3K27ac super-enhancer (SE) signals flanking the ZMYND8 locus across multiple neuroblastoma (NB) cell lines. Hi-C and Capture Hi-C analyses revealed chromatin interactions between this SE region and the ZMYND8 promoter. Luciferase reporter assays, combined with CRISPR/Cas9-mediated enhancer deletion, functionally validated E1 as a key regulatory enhancer. Targeted repression of E1 significantly reduced ZMYND8 expression and impaired NB cell proliferation. Both in vitro and in vivo experiments demonstrated that ZMYND8 knockdown suppressed proliferation and colony formation while inducing apoptosis in NB cells. RNA-seq analysis revealed that ZMYND8 depletion downregulated E2F target genes and transcripts associated with the G2/M checkpoint. By integrating RNA-seq, ATAC-seq, and CUT&Tag data, we identified CDK6 as a critical downstream effector within the ZMYND8-dependent transcriptional program. Finally, structure-based virtual screening identified HMN-176 as a candidate compound modulating the ZMYND8 pathway. HMN-176 reduced ZMYND8 protein levels without significantly altering its mRNA expression. The compound also downregulated CDK6 expression, induced apoptosis, and inhibited NB growth both in vitro and in vivo. Collectively, our findings delineate a BRD4/SE–ZMYND8–CDK6 regulatory axis that mechanistically links enhancer activity to cell-cycle control in neuroblastoma.

2. Materials and methods

2.1 Cell lines and cell culture

SK-N-BE(2), SK-N-AS and SH-SY5Y were obtained from the Cell Bank of Chinese Academy of Sciences. A murine neuroblastoma cell line was established from a primary tumor arising in an MYCN-driven transgenic mouse. SK-N-AS and SH-SY5Y were maintained in DMEM (L110KJ, BasalMedia, Shanghai, China), SK-N-BE(2) in DMEM/F-12 (L320KJ, BasalMedia, Shanghai, China), and murine

neuroblastoma cells in Neuroblastoma Conditional Reprogramming Medium (PRS-NBM-CR, Precedo, Hefei, China). All media were supplemented with 10% fetal bovine serum (F0193, Sigma-Aldrich, MO, USA) and penicillin/streptomycin (C0222, Beyotime, Shanghai, China). Cells were cultured at 37 °C in a humidified atmosphere with 5% CO_2. Cell line identity was confirmed by short tandem repeat (STR) profiling.

2.2 Generation of Stable Cell Lines for Gene Knockdown and Enhancer Silencing

To establish stable ZMYND8 knockdown cell lines, shRNAs specifically targeting ZMYND8 were designed and synthesized by IGE Biotechnology (Guangzhou, China). Lentiviral supernatants were produced from pLKO.1-puro plasmids expressing either scrambled control shRNA or ZMYND8-targeting shRNA, followed by transduction into SK-N-BE(2), SK-N-AS and SH-SY5Y cells. SK-N-BE(2) and SK-N-AS cells were first transduced with Cas9-expressing lentivirus and subjected to G418 selection to generate stable Cas9-expressing cell populations. sgRNAs against the candidate enhancer as well as non-targeting control sgRNA (sgNC) were separately cloned into the Lenticrispr-copGFP vector, with all constructs synthesized by IGE Biotechnology. The resultant sgRNA-loaded lentiviral particles were subsequently transduced into the Cas9-positive stable cell lines.

2.3 Dual Luciferase Reporter Assay

Candidate enhancer fragments E1 and E2 of ZMYND8 were cloned into the pGL3-Promoter luciferase reporter vector (Promega, WI, USA). The target recombinant vectors were co-transfected with the Renilla luciferase control vector into NB cells using Lipo8000 transfection reagent (C0533, Beyotime). After 48 h of post-transfection incubation, the Dual Luciferase Reporter Assay Kit (DL101, Vazyme, Nanjing, China) was utilized to detect the dual-luciferase reporter activity.

2.4 Cell viability assays

Cell viability was determined via the CCK-8 assay (K1018, APExBIO, TX, USA) following the manufacturer's protocol. For cell proliferation assays, ZMYND8-knockdown neuroblastoma cell lines (SK-N-BE(2), SK-N-AS, SH-SY5Y) were seeded in 96-well plates at 2×10^3 cells/150 μL and cultured at 37 °C with 5% CO_2.

CCK-8 reagent was added on days 1, 3, 5 and 7 post-seeding, followed by a 2 h incubation at 37 °C. For drug sensitivity assays, SK-N-BE(2) and SH-SY5Y cells were plated at 8×10^3 cells/150 μL. After attachment, cells were exposed to serially diluted compounds for 48 h prior to CCK-8 incubation (2 h, 37 °C). Absorbance was recorded at 450 nm on a microplate reader. IC_{50} values and relative cell viability were calculated using GraphPad Prism 10.

2.5 H3K27ac ChIP-seq data processing and super-enhancer identification

ChIP-seq reads were aligned to the hg38 human reference genome using Bowtie2 (version 2.4.2). ChIP-seq peaks were subsequently identified using Model-based Analysis for ChIP-Seq (MACS2, version 2.2.7.1) with default parameters. BigWig files were generated using the bedGraphToBigWig utility from the UCSC Genome Browser and visualized with the Integrative Genomics Viewer (IGV). Super-enhancers were identified using the Rank Ordering of Super-Enhancers (ROSE) algorithm. H3K27ac peaks located more than 2 kb from any transcription start site were defined as enhancer regions. Enhancer elements separated by less than 12.5 kb were stitched together, and stitched enhancers were ranked according to H3K27ac signal intensity. The inflection point at which the tangent slope equaled 1 was used as the threshold to distinguish typical enhancers from super-enhancers.

2.6 Capture Hi-C experiments and data analysis

Hi-C libraries were prepared using the EpiTect Hi-C Kit (59971, Qiagen, Venlo, Netherlands). Briefly, 2×10^6 cells were harvested and crosslinked with formaldehyde, cells were lysed, beads equilibrated to room temperature were added to bind nuclei, and all subsequent reactions were performed according to the manufacturer's instructions. Hybridization of the Hi-C libraries to a custom 120-mer biotinylated DNA probe pool (Dynegene Technologies) was performed using the QuarHyb Super DNA Reagent Kit (NC1009A, Dynegene, Shanghai, China); capture libraries were then enriched and amplified according to the manufacturer's protocol. Libraries were sequenced on an Illumina HiSeq PE150 platform to generate 2×150 bp paired-end reads. Raw reads were filtered using fastp, aligned to the human reference genome hg38 with Bowtie2, and

valid contact pairs were identified using HiC-Pro (v3.1.0) with default parameters[20]. Chromatin loops were called with hichipper (v0.7.7)[21], and visualization was performed with the R package plotgardener.

2.7 RNA-seq and Data Analysis

RNA-seq was performed according to the protocol provided by Novogene Bioinformatics Technology Co., Ltd. (Beijing, China). Differential expression analysis was performed using DESeq2, and differentially expressed genes (DEGs) were identified with the screening criteria of |log2FoldChange| > 1.0 and adjusted $P < 0.05$. Gene set enrichment analysis (GSEA) was conducted using the clusterProfiler package (version 4.4) in R version 4.2.1.

2.8 CUT&Tag

CUT&Tag assays were performed using the Hyperactive Universal CUT&Tag Assay Kit for Illumina (TD903, Vazyme) according to the manufacturer's instructions. The procedure included cell collection, primary- and secondary-antibody incubation, incubation with hyperactive pA/G transposase, tagmentation, DNA extraction, and library amplification. Purified libraries were sequenced by Novogene Bioinformatics Technology Co., Ltd.

2.9 ATAC-seq

ATAC-seq was performed using the indicated kit (TD501, Vazyme) according to the manufacturer's protocol with minor modifications. Briefly, cells were collected and lysed, followed by tagmentation, reaction termination, DNA extraction, library amplification, and size selection. Purified libraries were quality-controlled and sequenced by Novogene Bioinformatics Technology Co., Ltd.

2.10 In vivo experiments

All animal experiments were performed in accordance with institutional ethical guidelines and were approved by the Animal Care and Use Committee of Soochow University (approval number: CAM-SU-AP#: JP-2018-1; SUDA20251229A02).

Five-week-old female mice were randomly assigned to groups of five. Luciferase-

labeled neuroblastoma cells (5×10^6 cells/mouse) were subcutaneously inoculated to establish xenograft or syngeneic tumor models. For drug-treatment experiments, HMN-176 was administered intraperitoneally at 20 mg/kg. Tumor growth was monitored by caliper measurement and bioluminescence imaging.

2.11 Structure-based virtual screening

The crystal structure of human ZMYND8 (PDB ID: 4COS) was used for structure-based virtual screening. Potential ligand-binding sites were predicted using MOE, and Site 1 within the PWWP domain was selected as the docking pocket. The protein structure was prepared using the Protein Preparation Wizard in Schrödinger, including bond-order assignment, hydrogen addition, protonation at pH 7.0 using PROPKA, and restrained energy minimization with the OPLS4 force field. Compounds from the T001 known bioactive compound library were prepared using LigPrep. Protonation states were generated using Epik at pH 7.0 ± 2.0, salts were removed, and tautomeric and conformational states were generated while retaining the original stereochemistry, with up to 32 conformations generated per compound. Molecular docking was subsequently performed using the Glide standard-precision (SP) mode in Schrödinger. Compounds with docking scores below −7 kcal/mol were retained for further analysis. Protein–ligand interaction fingerprints (PLIFs) were analyzed, followed by structure-based clustering using the Jarvis–Patrick algorithm in MOE with a structural similarity threshold of 70%. Representative compounds with favorable docking scores from each cluster were further visually inspected for binding mode and structural plausibility. Finally, 156 candidate compounds were selected for subsequent experimental validation.

2.12 Statistical analysis

All experiments were performed independently, with at least three biological replicates for each condition. For time-course experiments, statistical comparisons were performed using endpoint measurements unless otherwise indicated. Statistical analyses were primarily conducted using unpaired two-tailed Student's t-test or one-way analysis of variance (ANOVA), and data were analyzed using GraphPad Prism 10.

Differential expression analysis of RNA-seq data was corrected for multiple testing using the false discovery rate (FDR). Statistical significance was indicated as follows: ns, not significant; *P < 0.05; **P < 0.01; ***P < 0.001; and ****P < 0.0001. All error bars represent standard deviations (SD), with n ≥ 3.

Additional experimental procedures and bioinformatic analyses are provided in the **Supplementary Methods.**

3. Results

3.1 Identification of ZMYND8 as a Super-Enhancer-Regulated Gene in Neuroblastoma

Super-enhancers (SEs) are large cis-regulatory elements defined by extensive enrichment of active histone modifications—most notably H3K27ac—and play pivotal roles in sustaining tumor-specific transcriptional programs and driving the expression of key oncogenes. As a central epigenetic reader, BRD4 is critically involved in SE-mediated transcriptional regulation and governs the expression of several essential oncogenes, including MYCN, in neuroblastoma (NB). In our prior studies, the BRD4-targeting PROTAC degraders dBET57 and GNE-987 potently suppressed NB cell proliferation, induced apoptosis and cell-cycle arrest, and profoundly remodeled the SE landscape in NB cells[14,16]. Through integrated RNA-seq and ChIP-seq analyses, we further identified ZMYND8 as a SE-associated downstream gene whose expression was significantly altered upon dBET57 treatment[16].

To systematically determine whether ZMYND8 is under super-enhancer regulation in neuroblastoma, we integrated H3K27ac ChIP-seq datasets from 25 NB cell lines and 7 NB patients, and found that ZMYND8 is frequently regulated by super-enhancers (Figure 1A). Enhancer ranking based on H3K27ac signal intensity revealed that ZMYND8 was consistently associated with super-enhancers (SEs) across multiple neuroblastoma (NB) cell lines—mirroring the SE association patterns observed for other NB lineage–defining transcription factors, including MEIS2, HAND2, GATA3, and PHOX2B (Figure 1B; Figure S1A). Visualization of H3K27ac ChIP-seq profiles

using the Integrative Genomics Viewer (IGV) further confirmed robust H3K27ac enrichment flanking the ZMYND8 locus in the majority of NB cell lines (Figure 1C; Figure S1A). Moreover, analysis of publicly available transcriptomic data from the Th-MYCN$^{+/+}$ mouse model demonstrated that Zmynd8 expression was significantly elevated in sympathetic ganglia of Th-MYCN$^{+/+}$ mice relative to wild-type controls and exhibited coordinated expression with multiple established NB-associated genes (Figure 1D). Given the well-documented role of BRD4 in regulating transcription at SE-driven loci, we next investigated whether BRD4 modulates ZMYND8 expression. BRD4 knockdown in SK-N-BE(2) and SK-N-AS cells led to a significant reduction in ZMYND8 expression at both the mRNA and protein levels (Figure 1E–F). Consistently, pharmacological inhibition of BRD4 with GNE-987 markedly decreased ZMYND8 protein abundance in both NB cell lines (Figure 1G). Together with our prior observations following dBET57 treatment and the current chromatin-level validation, these findings establish ZMYND8 as a bona fide NB-associated gene under direct regulation by the BRD4–super-enhancer axis.

3.2 The Core Enhancer E1 Mediates SE-Dependent Regulation of ZMYND8 Expression

To further delineate the regulatory mechanism by which the ZMYND8-associated super-enhancer (SE) controls its target gene, we first examined chromatin interactions between the ZMYND8-SE region and the ZMYND8 promoter. Leveraging our SK-N-BE(2) Hi-C dataset, we performed promoter-focused Capture Hi-C to enhance sequencing depth specifically at the ZMYND8 locus. A robust chromatin loop interaction was detected between the ZMYND8-SE region and the ZMYND8 promoter (Figure 2A), supporting a spatial proximity between this enhancer region and its cognate promoter. Next, we selected two candidate enhancer regions—E1 and E2—based on the distribution of H3K27ac peaks across the ZMYND8-SE region. These regions, along with a negative-control genomic region, were cloned into the pGL3-promoter luciferase reporter vector and assayed in both SK-N-BE(2) and SK-N-AS cells (Figure 2B). E1 conferred a marked increase in luciferase activity—consistent

with its strong H3K27ac enrichment—whereas E2 exhibited only minimal transcriptional activation. Collectively, these results identify E1 as a candidate core functional element within the ZMYND8-SE.

To validate the functional role of enhancer E1 in cellular contexts, we employed CRISPR/Cas9-mediated enhancer disruption to specifically ablate the E1 cis-regulatory element. Two independent single-guide RNA (sgRNA) pairs—sgRNA1+2 and sgRNA3+4—were designed to target distinct sites within the E1 region (Figure 2C). Both sgRNA combinations induced significant reductions in ZMYND8 expression at both the mRNA and protein levels (Figure 2D–E). Consistent with these molecular phenotypes, repression of E1 markedly impaired the proliferative capacity of SK-N-BE(2)-Cas9 and SK-N-AS-Cas9 cells, whereas treatment with control sgRNAs exerted no discernible effect (Figure 2F). Notably, E1 repression did not significantly affect the proliferation of parental SK-N-BE(2) and SK-N-AS cells lacking Cas9 expression (Figure 2F). Collectively, these results demonstrate that the core enhancer E1 within the ZMYND8 super-enhancer is essential for transcriptional activation of ZMYND8 and supports neuroblastoma (NB) cell proliferation.

3.3 ZMYND8 Promotes NB Cell Proliferation In Vitro and In Vivo

To investigate the biological function of ZMYND8 in neuroblastoma (NB), we designed three short hairpin RNAs (shRNAs) specifically targeting ZMYND8 (sh-ZMYND8#1, #2, and #3) alongside a non-targeting control shRNA (sh-NC). These constructs were stably transduced into SK-N-BE(2), SK-N-AS, and SH-SY5Y NB cell lines. Western blotting and RT-qPCR analyses confirmed that sh-ZMYND8#1 and sh-ZMYND8#2 effectively suppressed ZMYND8 expression at both the mRNA and protein levels across all three cell lines (Figure 3A–B; Supplementary Figure 2A–B). Compared with the sh-NC control, ZMYND8 knockdown significantly inhibited cellular proliferation in SK-N-BE(2), SK-N-AS, and SH-SY5Y cells ($P < 0.01$) (Figure 3C–D; Supplementary Figure 2C–D). Consistently, colony formation assays revealed a substantial decrease in clonogenic capacity upon ZMYND8 depletion, as reflected by both reduced colony number and diminished colony size (Figure 3E; Supplementary

Figure 2E). Furthermore, Annexin V-FITC/propidium iodide (PI) staining coupled with flow cytometric analysis demonstrated a significant increase in the proportion of apoptotic cells following ZMYND8 knockdown (Figure 3F). Supporting this observation, Western blot analysis showed elevated levels of cleaved PARP—a hallmark of caspase-mediated apoptosis—upon ZMYND8 depletion (Supplementary Figure 2F). Collectively, these findings indicate that ZMYND8 promotes NB cell proliferation and clonogenicity while exerting an anti-apoptotic function.

To determine whether ZMYND8 modulates neuroblastoma (NB) tumor growth in vivo, we established a subcutaneous xenograft model in immunodeficient nude mice. Luciferase-labeled SK-N-BE(2) cells stably expressing either ZMYND8-targeting shRNA or non-targeting control shRNA (sh-NC) were inoculated subcutaneously into the right flank of each mouse. Tumor growth was monitored longitudinally via bioluminescence imaging (BLI) (Figure 4A). Three weeks post-inoculation, BLI signal intensity was markedly diminished in the ZMYND8-knockdown group relative to the sh-NC control group (Figure 4B–C). Consistently, serial caliper-based tumor volume measurements revealed significantly attenuated tumor growth upon ZMYND8 depletion (Figure 4D), and tumors harvested at the experimental endpoint weighed significantly less in the knockdown group than in controls (Figure 4E–G). Western blotting and immunohistochemical analyses of xenograft tissues confirmed efficient ZMYND8 knockdown and further demonstrated a significant reduction in the proportion of Ki-67–positive proliferating tumor cells (Figure 4H–J). Collectively, these in vivo findings corroborate the in vitro results and establish that ZMYND8 depletion suppresses NB tumorigenesis in vivo.

3.4 ZMYND8 Sustains Cell Cycle Progression and CDK6-Mediated Transcriptional Programs in Neuroblastoma

To investigate the transcriptional mechanisms underlying ZMYND8-dependent neuroblastoma (NB) cell proliferation, we performed RNA-seq analysis on SK-N-BE(2) cells transduced with either non-targeting control shRNA (sh-NC) or ZMYND8-targeting shRNA. Differential expression analysis identified 862 downregulated and

841 upregulated genes upon ZMYND8 depletion ($|\log_2 FC| > 1$, adjusted *P* < 0.05) (Figure 5A). Gene set enrichment analysis (GSEA) of the downregulated gene set revealed significant suppression of E2F target genes and the G2/M checkpoint pathway following ZMYND8 knockdown (Figure 5B–D). Further interrogation showed that multiple key NB-associated oncogenes and lineage-specific regulators were significantly downregulated upon ZMYND8 depletion (Figure 5E). These transcriptional changes were independently confirmed by RT-qPCR and Western blot analyses (Figure 5F–G). Collectively, these findings indicate that ZMYND8 sustains transcriptional programs essential for cell-cycle progression and proliferative capacity in NB cells.

To systematically identify key downstream effectors of ZMYND8, we performed RNA-seq and ATAC-seq in SK-N-BE(2) neuroblastoma cells with or without ZMYND8 depletion. In parallel, we conducted CUT&Tag to map the genome-wide chromatin occupancy of ZMYND8 in neuroblastoma cells. Differentially expressed genes, genes associated with altered chromatin accessibility, and ZMYND8-bound target genes were independently identified using predefined criteria (Figure 6A). CUT&Tag analysis revealed that approximately 50% of ZMYND8-binding peaks localized to promoter regions, indicating a role for ZMYND8 in promoter-associated transcriptional regulation (Figure 6B, Supplementary Figure 3A–B). Consistent with this, ATAC-seq analysis demonstrated a widespread reduction in chromatin accessibility upon ZMYND8 depletion (Figure 6C, Supplementary Figure 3C–D). Integrative analysis further showed that chromatin accessibility at ZMYND8-bound loci was significantly diminished following ZMYND8 knockdown (Figure 6D). Among the 84 candidate target genes identified through integrative analysis, CDK6 emerged as a top candidate (Figure 6E). CDK6 is a critical regulator of cell-cycle progression and has been reported to be aberrantly overexpressed in high-risk neuroblastoma, where it drives malignant proliferation.

Further analysis of the ZMYND8 CUT&Tag dataset revealed a prominent ZMYND8-bound regulatory enhancer that is functionally linked to CDK6 expression (Figure 6F). In addition, ZMYND8 occupancy was detected at regulatory regions

proximal to other neuroblastoma-associated genes—including PHOX2B and NFIB (Supplementary Figure 4A–B)—suggesting a broader role for ZMYND8 in transcriptional regulation. Nevertheless, given the robust multi-omics evidence and functional significance of CDK6 within this context, we prioritized the ZMYND8–CDK6 regulatory axis for subsequent investigation. To assess its functional relevance, we employed a CRISPR-Cas9–mediated genomic deletion strategy to excise this enhancer. Enhancer ablation led to a pronounced reduction in CDK6 protein levels and significantly impaired the proliferation of SK-N-BE(2)-Cas9 cells (Figure 6G–I). In contrast, no discernible effect on proliferation was observed in the corresponding control cells (Figure 6J). Collectively, these findings establish CDK6 as a key downstream effector in the ZMYND8-associated transcriptional regulatory network and provide direct functional evidence linking ZMYND8-dependent chromatin regulation to CDK6 expression in neuroblastoma cells.

3.5 Virtual Screening Identifies HMN-176 as a Candidate Compound Associated with ZMYND8 signaling in NB

ZMYND8 plays a critical role in the assembly of transcriptional regulatory complexes and has been implicated in chromatin “reading” and the DNA damage response. Recent studies further indicate that ZMYND8 cooperates with epigenetic regulators—including KDM5C—to modulate enhancer activity. Human ZMYND8 is an 1,186-amino-acid protein; the available 4COS crystal structure (PDB ID: 4COS) spans residues 83–406 and encompasses tandem PHD and bromodomain (BRD) modules, as well as a zinc-finger motif that links the PHD/BRD region to the PWWP domain. Structural alignment using Molecular Operating Environment (MOE) yielded a root-mean-square deviation (RMSD) of 0.793 Å. We employed the 4COS structure of ZMYND8 as the structural template for virtual screening. Following protonation and energy-based structural optimization, potential ligand-binding pockets on the protein surface were systematically identified and characterized; the most promising pocket—selected based on druggability, conservation, and proximity to functionally relevant motifs—was used for subsequent compound screening. Multiple ligand conformations

were generated and docked into the optimized protein structure using Schrödinger's Glide software. Candidate compounds were then prioritized according to three key criteria: predicted binding affinity (expressed as docking score), structural diversity (assessed via fingerprint-based clustering), and binding mode compatibility (e.g., formation of key hydrogen bonds or hydrophobic interactions with conserved residues). This integrated prioritization strategy (Figure 7A; Supplementary Figures 5 and 6A–F) yielded a final set of 156 compounds exhibiting favorable predicted binding properties.

Among the candidate compounds prioritized on the basis of docking scores, interaction profiles, structural diversity, and binding-mode analyses, HMN-176 and PKD-IN-1 demonstrated potent inhibitory effects on neuroblastoma (NB) cell viability (Supplementary Figure 7A). IC_{50} analysis revealed that HMN-176 exhibited superior cellular inhibitory activity compared with PKD-IN-1, as evidenced by its significantly lower IC_{50} value (Figure 7B). Notably, HMN-176 reduced ZMYND8 protein abundance in a concentration-dependent manner at relatively low concentrations, without significantly altering ZMYND8 mRNA levels (Figure 7C–D). Consistent with the phenotypic effects observed upon ZMYND8 knockdown, HMN-176 treatment induced dose-dependent increases in NB cell death and suppressed colony-forming capacity (Supplementary Figure 7B–C). Furthermore, HMN-176 treatment promoted apoptosis, enhanced PARP cleavage, and decreased CDK6 protein expression (Supplementary Figure 7D; Figure 7E).

We next assessed the in vivo antitumor efficacy of HMN-176 using a subcutaneous SK-N-BE(2) xenograft model. Luciferase-expressing SK-N-BE(2) cells were implanted subcutaneously into mice, and HMN-176 was administered intraperitoneally at 20 mg/kg once daily from day 5 to day 16, excluding days scheduled for bioluminescence imaging (BLI). Tumor growth was longitudinally monitored by BLI on days 7, 14, and 21 (Figure 7F). Relative to vehicle-treated controls, HMN-176–treated mice exhibited significantly attenuated bioluminescent signals (Figure 7G, Supplementary Figure 8A). Body weight was measured on days 3, 6, 12, and 18, and no statistically significant differences were observed between the two groups (Figure 7H), indicating absence of treatment-related systemic toxicity. Consistent with the BLI

data, HMN-176–treated mice developed significantly smaller tumors compared with vehicle-treated controls (Figure 7I–J, Supplementary Figure 8B). Hematoxylin and eosin (H&E) staining and immunohistochemical (IHC) analysis further revealed downregulated ZMYND8 expression in tumors from HMN-176–treated mice, accompanied by corresponding histopathological alterations (Supplementary Figure 8C–D). Histopathological examination of liver and kidney tissues showed no discernible pathological abnormalities (Figure 7K), collectively suggesting that HMN-176 was well tolerated under the dosing regimen employed in this study.

3.6 Zmynd8 promotes and HMN-176 suppresses murine neuroblastoma growth

To further assess the therapeutic potential of Zmynd8-targeted therapy in murine neuroblastoma models, we utilized a murine neuroblastoma cell line derived from a primary tumor that arose in an MYCN-driven transgenic mouse. Genetic depletion of ZMYND8 markedly suppressed cellular proliferation (Figure 8A–C). Consistently, treatment with HMN-176 reduced ZMYND8 protein levels and significantly inhibited the growth of murine neuroblastoma cells (Figure 8D–E). Next, we established a syngeneic subcutaneous neuroblastoma model in C57BL/6 mice using luciferase-expressing murine neuroblastoma cells, followed by administration of HMN-176 (Figure 8F). In line with findings from the human neuroblastoma xenograft model, HMN-176 treatment led to a significant reduction in tumor bioluminescence imaging (BLI) signal intensity and effectively suppressed tumor growth relative to vehicle-treated controls (Figure 8G–H). Body weight measurements taken on days 3, 6, 12, and 16 revealed no statistically significant differences between the two groups (Figure 8I), indicating absence of overt systemic toxicity. Consistent with these observations, HMN-176–treated mice developed significantly smaller tumors than vehicle-treated controls (Figure 8J). Histopathological examination of liver and kidney tissues showed no apparent pathological abnormalities (Figure 8K), further supporting the conclusion that HMN-176 did not induce notable systemic toxicity under the experimental dosing regimen employed in this study.

Collectively, both genetic and pharmacological evidence support an oncogenic role for ZMYND8 in neuroblastoma and demonstrate that HMN-176 exerts potent antitumor activity in both human-derived and murine neuroblastoma models. BRD4-dependent super-enhancers drive ZMYND8 transcription, and ZMYND8, in turn, sustains the CDK6-associated transcriptional program to promote neuroblastoma cell proliferation and survival. HMN-176 downregulates ZMYND8 protein levels and represses CDK6 expression, thereby inducing apoptosis and suppressing tumor growth (Figure 8L).

4. Discussion

Neuroblastoma exhibits pronounced genetic and epigenetic heterogeneity, and its growth is critically dependent on lineage-specific transcriptional programs. Beyond canonical genetic alterations—including MYCN amplification and ALK activation—dysregulated enhancer activity has emerged as a key driver of neuroblastoma (NB) pathobiology[1-3]. Prior super-enhancer (SE) profiling studies have delineated two major cellular states in NB: adrenergic/noradrenergic and mesenchymal. These studies further uncovered core transcriptional regulatory networks centered on PHOX2B, HAND2, GATA3, ISL1, TBX2, and MYCN[4-6,22-24]. Importantly, these cellular states are dynamic rather than fixed; NB cells can reversibly transition between adrenergic and mesenchymal identities in response to extrinsic signaling cues and microenvironmental changes—a plasticity that may significantly influence therapeutic response[22,25,26]. Moreover, BRD4-dependent transcription plays a pivotal role in sustaining both MYCN-driven and core regulatory circuitry (CRC)-driven transcriptional programs in NB[6,14,16,27,28]. The identification of SE-regulated oncogenic effectors—such as FAM163A and IRF2BP2—further underscores that super-enhancers promote NB progression not only by reinforcing lineage-defining transcription factors but also by directly activating downstream effector genes[14,15]. In this study, we identify ZMYND8 as an additional SE-regulated gene in NB. Our data establish a BRD4/SE–ZMYND8–CDK6 regulatory axis that mechanistically links enhancer activity to cell-cycle control.

Multiple lines of evidence collectively demonstrate that ZMYND8 expression is regulated in a super-enhancer (SE)-dependent manner in neuroblastoma. H3K27ac profiling reveals robust super-enhancer signals flanking the ZMYND8 locus across multiple neuroblastoma (NB) cell lines. Hi-C and promoter-focused Capture Hi-C analyses further confirm spatial chromatin interactions between this super-enhancer region and the ZMYND8 promoter. Functional dissection identifies E1 as the core regulatory element within the super-enhancer: E1 exhibits potent enhancer activity, and its genetic disruption significantly downregulates ZMYND8 expression and impairs neuroblastoma cell proliferation. Moreover, both BRD4 knockdown and pharmacological inhibition of BRD4 markedly suppress ZMYND8 expression, underscoring the dependence of ZMYND8 transcription on BRD4-mediated enhancer function. These findings align with prior studies showing that SE-regulated genes exhibit heightened sensitivity to perturbations in enhancer transcription and are critically reliant on transcriptional co-activators such as BRD4[10-12,27-29]. Collectively, these results establish a functional—rather than merely correlative—relationship between ZMYND8 expression and super-enhancer activity, extending beyond passive H3K27ac enrichment. Thus, ZMYND8 is positioned as a key component of a BRD4-dependent transcriptional program in neuroblastoma.

ZMYND8 is particularly intriguing because it functions as a chromatin reader. Its PHD–BRD–PWWP domain module recognizes multiple chromatin features, thereby facilitating the recruitment of ZMYND8 to specific genomic loci[17]. Early studies primarily focused on the role of ZMYND8 in the DNA damage response, where it contributes to the recruitment and/or regulation of the NuRD complex at sites of chromatin damage[18,30,31]. Subsequent investigations have revealed broader roles for ZMYND8 in transcriptional regulation. Notably, ZMYND8 interacts with P-TEFb and participates in transcriptional elongation[19]. In breast cancer, ZMYND8 has been shown to support HIF-dependent transcription by promoting BRD4 recruitment and enhancing RNA polymerase II elongation[32,33]. Additional studies have linked ZMYND8 to oncogenic transcription, cancer stem cell maintenance, and therapy resistance across diverse tumor contexts[34-36]. Collectively, these findings underscore the context-

dependent functionality of ZMYND8. Our study extends this paradigm to neuroblastoma (NB). We demonstrate that ZMYND8 supports NB proliferation and survival: depletion of ZMYND8 significantly impairs cellular proliferation and colony-forming capacity, induces apoptosis, and suppresses tumor growth in vivo.Our results further establish a functional link between ZMYND8 and cell-cycle regulation. RNA-seq analysis revealed that ZMYND8 depletion markedly downregulates E2F target genes and genes associated with the G2/M checkpoint. Dysregulation of cell-cycle checkpoints is a well-characterized hallmark of NB, and aberrant activation of the cyclin D–CDK4/6 signaling axis contributes critically to sustaining the proliferative, poorly differentiated phenotype[37-39]. Prior work has demonstrated that elevated cyclin D1 expression and CDK4 activity correlate with the undifferentiated state of NB cells; moreover, pharmacological inhibition of CDK4/6 induces cell-cycle arrest and senescence[37,38]. Consequently, CDK4/6 inhibitors have emerged as promising therapeutic candidates for NB[38,39]. More recently, palbociclib—a selective CDK4/6 inhibitor—has been shown to promote neuronal differentiation in adrenergic NB cells[40]. These prior findings provide a compelling biological rationale for our observation that CDK6 represents a key downstream effector of ZMYND8.

We integrated RNA-seq, ATAC-seq, and ZMYND8 CUT&Tag data to identify genes whose expression depends on ZMYND8. CDK6 emerged as one of the most robust candidates from this integrative analysis. Depletion of ZMYND8 significantly reduced chromatin accessibility at genomic regions bound by ZMYND8. Furthermore, we identified a distal enhancer associated with the CDK6 locus that is directly occupied by ZMYND8. CRISPR-mediated deletion of this enhancer diminished CDK6 expression and suppressed neuroblastoma (NB) cell proliferation. These findings indicate that ZMYND8 contributes to maintaining a transcriptionally permissive chromatin state at key cell-cycle–regulated genes, with CDK6 representing a critical downstream effector within this regulatory program. Nevertheless, CDK6 is unlikely to account for the full spectrum of phenotypic consequences resulting from ZMYND8 loss. Indeed, ZMYND8 knockdown induced widespread alterations in chromatin accessibility and dysregulated numerous E2F- and G2/M-phase–associated genes,

suggesting that ZMYND8 governs a broader transcriptional network. Rescue experiments—specifically, re-expression of CDK6 in ZMYND8-depleted cells—would help delineate the extent to which CDK6 mediates the observed proliferative defects. Moreover, given the previously reported physical and functional interactions of ZMYND8 with multiple epigenetic regulators—including the NuRD complex, P-TEFb, BRD4, and others[18,19,28-34], defining the precise composition and context-specific assembly of ZMYND8-associated transcriptional complexes in NB will be essential for elucidating the mechanistic basis of ZMYND8-dependent enhancer activation and downstream gene regulation.

The identification of HMN-176 represents an initial pharmacological approach for modulating the ZMYND8-associated regulatory pathway. Structure-based virtual screening identified HMN-176 as a top candidate compound, and subsequent experimental validation demonstrated that HMN-176 significantly reduced ZMYND8 protein levels without markedly affecting its mRNA expression. This reduction was associated with decreased CDK6 expression, enhanced apoptosis, impaired clonogenic capacity, and suppression of neuroblastoma (NB) tumor growth in preclinical models. However, HMN-176 is not a validated, selective inhibitor of ZMYND8. Prior studies have documented multiple off-target activities of both HMN-176 and its prodrug HMN-214. Specifically, HMN-176 has been shown to interfere with NF-Y–dependent transcription and to modulate MDR1 expression[41]. HMN-214, meanwhile, has been implicated in PLK1-mediated mitotic regulation[42,43] and has demonstrated antitumor activity in NB models through inhibition of PLK1 function[43]. Thus, although the observed downregulation of ZMYND8 protein upon HMN-176 treatment suggests a potential contribution of ZMYND8 to the compound's antineuroblastoma activity, the present findings do not establish ZMYND8 as the direct or exclusive molecular target of HMN-176.

Further pharmacological characterization will therefore be required. Biophysical binding assays, cellular target-engagement studies, protein-stability analyses, and structure-guided mutagenesis would collectively help determine whether HMN-176 directly interacts with ZMYND8. In parallel, genetic experiments—such as modulation

of endogenous ZMYND8 expression or introduction of drug-resistant ZMYND8 mutants—will be essential to assess whether alterations in ZMYND8 levels or function modulate cellular sensitivity to HMN-176, thereby providing more robust evidence for target dependency. Pharmacokinetic and toxicological profiling will also be necessary, notwithstanding the absence of overt body-weight loss or major histopathological abnormalities under the treatment conditions employed in this study. Finally, given that BRD4-dependent transcription, MYCN signaling, and CDK4/6-mediated cell-cycle progression represent interconnected therapeutic vulnerabilities in neuroblastoma (NB)[6,14,16,25,26,35-39], it will be critical to evaluate whether pharmacological or genetic perturbation of ZMYND8 synergizes with BET inhibition, CDK4/6 inhibition, differentiation therapy, or standard cytotoxic regimens.

In summary, the present study systematically identifies ZMYND8 as a novel super-enhancer-driven chromatin regulator that critically promotes the malignant progression of neuroblastoma. Mechanistically, ZMYND8 is transcriptionally controlled by a BRD4-dependent super-enhancer, and functions to maintain open chromatin states at key cell-cycle gene loci. By directly binding and activating the distal enhancer of CDK6, ZMYND8 sustains E2F and G2/M checkpoint transcriptional programs, thereby facilitating NB cell proliferation and tumor growth. Pharmacologically, the small-molecule compound HMN-176 exhibits potent anti-tumor effects in NB models potentially through downregulating ZMYND8 and its downstream CDK6 signaling. Additional studies are warranted to quantify the extent to which CDK6 contributes to ZMYND8-dependent tumor growth and to definitively establish whether HMN-176 engages ZMYND8 directly. Collectively, this work defines a previously unrecognized BRD4/SE–ZMYND8–CDK6 regulatory axis, expands the understanding of super-enhancer-mediated oncogenic transcription in neuroblastoma, and highlights ZMYND8 as a viable and promising therapeutic target for NB treatment.

Funding

This work was supported by grants from the National Natural Science Foundation (82573841, 82373414, 82404067, 82573025), Jiangsu Provincial Health Commission Scientific Research Project (H2023142), the Science and Technology Development Project of Suzhou City (SYW2024024, SYW2024105, SYW2024111), and National Outstanding Youth Cultivation Program Project (YYJQ004); the Suzhou Science and Education Strengthening Health Program (Youth Project) (QNXM2024026); the Suzhou Applied Basic Research (Medical and Health) Science and Technology Innovation Project—Youth Program (SYW2025116); and the China Postdoctoral Science Foundation (2025M782206).

Conflict of interest

The authors declare that they have no conflict of interest.

Author Contributions

Y.F.T., Z.M.Z. and J.P. designed and directed the study, supervised the writing of the paper; D.W., C.Y., L.X., Y.L.C. and R.Z. performed most of the experiments, analyzed the data, and wrote the manuscript ; G.L., X.L.L. and Y.Y. undertook public dataset mining and statistical analyses; J.J.Y., J.C., and X.L. helped with RNA-seq, CUT&Tag and ATAC-seq experiments; C.X.S., T.L., L.L.H. and J.S.L. completed some of the in vivo studies. All authors contributed to this work and approved the final submitted version.

Data availability

The RNA-seq, ATAC-seq, and CUT&Tag datasets generated in this study have been deposited in the Gene Expression Omnibus (GEO) under accession number GSE345040.

Figure legends

Figure 1. Identification of ZMYND8 as a super-enhancer-regulated gene in neuroblastoma. (A) H3K27ac ChIP-seq data from 25 NB cell lines and 7 NB patients were integrated to profile enhancer activity around ZMYND8. **(B)** Rank ordering of super-enhancers based on H3K27ac ChIP-seq signals in representative neuroblastoma (NB) cell lines. ZMYND8 is highlighted. **(C)** Integrative Genomics Viewer (IGV) tracks showing H3K27ac enrichment surrounding the ZMYND8 locus in representative NB cell lines. The super-enhancer-associated region is indicated. **(D)** Expression analysis of Zmynd8 and representative NB-associated genes in sympathetic ganglia derived from Th-MYCN^+/+ and wild-type mice using publicly available datasets. **(E)** RT-qPCR analysis of ZMYND8 mRNA expression in SK-N-BE(2) and SK-N-AS cells following BRD4 knockdown. **(F)** Western blot analysis of BRD4 and ZMYND8 protein expression following BRD4 knockdown in SK-N-BE(2) and SK-N-AS cells. **(G)** Western blot analysis showing ZMYND8 protein abundance in SK-N-BE(2) and SK-N-AS cells following treatment with the BRD4 inhibitor GNE-987. Data are presented as mean±SD from three independent experiments. Unpaired two-tailed Student's t-test was performed. "ns" indicates not significant; *P < 0.05, **P < 0.01, ***P < 0.001, ****P < 0.0001.

Figure 2. The core enhancer E1 mediates super-enhancer-dependent transcriptional regulation of ZMYND8. (A) Chromatin interaction map of the ZMYND8 locus generated by Hi-C and promoter-focused Capture Hi-C in SK-N-BE(2) cells. A prominent chromatin interaction is observed between the ZMYND8-associated super-enhancer region and the ZMYND8 promoter. **(B)** Schematic representation of candidate enhancer regions E1 and E2 within the ZMYND8-associated super-enhancer and luciferase reporter analysis of their transcriptional activity in SK-N-BE(2) and SK-N-AS cells. A genomic region lacking prominent H3K27ac enrichment was used as a negative control. **(C)** Schematic illustration of the CRISPR/Cas9-mediated strategy used to disrupt the E1 enhancer. Two independent sgRNA combinations, sgRNA1+2 and sgRNA3+4, were designed to target E1. **(D)** RT-

qPCR analysis of ZMYND8 expression following CRISPR/Cas9-mediated disruption of E1. **(E)** Western blot analysis of ZMYND8 protein levels following E1 disruption. **(F)** Cell proliferation analysis of SK-N-BE(2)-Cas9, SK-N-AS-Cas9, parental SK-N-BE(2), and parental SK-N-AS cells following E1-targeting sgRNA treatment. Unpaired two-tailed Student's t-test and one-way ANOVA were performed. "ns" indicates not significant; *P < 0.05, **P < 0.01, ***P < 0.001, ****P < 0.0001.

Figure 3. ZMYND8 Promotes NB Cell Proliferation In Vitro. (A) RT-qPCR analysis confirming reduced ZMYND8 mRNA expression following ZMYND8 knockdown in NB cells. (B) Western blot analysis of ZMYND8 protein expression in SK-N-BE(2), SK-N-AS, and SH-SY5Y cells transduced with a non-targeting control shRNA (sh-NC) or independent ZMYND8-targeting shRNAs. (C–D) Cell proliferation assays showing reduced growth of NB cells following ZMYND8 depletion compared with sh-NC controls. (E) Representative images and quantitative analysis of colony formation assays showing decreased clonogenic capacity following ZMYND8 knockdown. (F) Flow cytometric analysis of apoptosis using Annexin V-FITC/PI staining in control and ZMYND8-depleted NB cells. Data are presented as mean±SD from three independent experiments. Unpaired two-tailed Student's t-test and one-way ANOVA were performed. "ns" indicates not significant; *P < 0.05, **P < 0.01, ***P < 0.001, ****P < 0.0001.

Figure 4. ZMYND8 Promotes NB Cell Proliferation In Vivo. Schematic representation of the subcutaneous xenograft model. Luciferase-labeled SK-N-BE(2) cells stably expressing sh-NC or ZMYND8-targeting shRNA were implanted subcutaneously into nude mice, and tumor progression was monitored longitudinally. **(B-C)** Representative bioluminescence imaging (BLI) and quantitative analysis of tumor-bearing mice in the control and ZMYND8-knockdown groups. **(D)** Tumor growth curves based on serial caliper measurements showing reduced tumor growth following ZMYND8 depletion. **(E)** Representative images of excised tumors at the experimental endpoint. **(F–G)** Quantification of tumor size and tumor weight at the

endpoint in control and ZMYND8-knockdown groups. **(H)** Western blot analysis confirming reduced ZMYND8 protein abundance in ZMYND8-knockdown xenograft tissues. **(I-J)** Representative immunohistochemical staining and quantitative statistics for ZMYND8 and Ki-67 in xenograft tumors. Data are presented as mean ± SD (n = 5 mice per group). Unpaired two-tailed Student's t-test was performed. "ns" indicates not significant; *P < 0.05, **P < 0.01, ***P < 0.001, ****P < 0.0001.

Figure 5. ZMYND8 promotes E2F target and G2/M checkpoint transcriptional programs. (A) Volcano plot showing differentially expressed genes in SK-N-BE(2) cells following ZMYND8 knockdown. A total of 862 genes were downregulated and 841 genes were upregulated according to the indicated differential-expression criteria. **(B)** Gene set enrichment analysis (GSEA) demonstrating significant suppression of E2F target genes following ZMYND8 depletion. **(C)** GSEA showing downregulation of the G2/M checkpoint transcriptional program in ZMYND8-depleted cells. **(D)** Representative visualization of genes within the E2F target and G2/M checkpoint gene sets. **(E)** Expression profile of multiple key neuroblastoma (NB)-associated genes significantly downregulated following ZMYND8 knockdown. **(F)** RT-qPCR validation of selected key neuroblastoma (NB)-associated genes identified by RNA-seq. **(G)** Western blot analysis confirming corresponding changes in representative key neuroblastoma (NB)-associated proteins following ZMYND8 depletion. Unpaired two-tailed Student's t-test was performed. "ns" indicates not significant; *P < 0.05, **P < 0.01, ***P < 0.001, ****P < 0.0001.

Figure 6. ZMYND8 Sustains a CDK6-Associated Transcriptional Program in NB Cells. (A) Schematic diagram of multi-omics integrative analysis for screening candidate target genes regulated by ZMYND8. **(B)** Genomic distribution of ZMYND8 CUT&Tag peaks, showing that approximately 50% of ZMYND8-binding sites are located in promoter regions. **(C)** Volcano plot from ATAC-seq assay showing reduced chromatin accessibility at most sites upon ZMYND8 knockdown. **(D)** ATAC-seq signals at ZMYND8-bound regions, indicating decreased chromatin accessibility

following ZMYND8 depletion. **(E)** The intersection of differentially expressed genes, genes with altered chromatin accessibility and ZMYND8-bound genes yielded 84 candidate target genes dependent on ZMYND8 regulation. **(F)** Genome browser view displaying ZMYND8 occupancy and chromatin features at the regulatory enhancer region associated with the CDK6 locus. **(G)** Generation of cells with CRISPR-Cas9-mediated deletion of the CDK6-associated enhancer. **(H)** Western blot results showing decreased CDK6 protein level after deletion of the CDK6-associated enhancer in SK-N-BE(2)-Cas9 cells. **(I)** Cell proliferation assay: SK-N-BE(2)-Cas9 cells exhibited impaired proliferative capacity upon enhancer deletion compared with control cells. **(J)** No obvious change in proliferative capacity was observed in SK-N-BE(2) cells after deletion of this enhancer. Unpaired two-tailed Student's t-test and one-way ANOVA were performed. "ns" indicates not significant; *P < 0.05, **P < 0.01, ***P < 0.001, ****P < 0.0001.

Figure 7. Virtual Screening Identifies HMN-176 as a Candidate Compound Associated with ZMYND8 signaling in NB. (A) Structure-based virtual screening workflow for candidate compounds predicted to interact with ZMYND8. **(B)** IC_{50} analysis comparing the effects of HMN-176 and PKD-IN-1 on neuroblastoma cell viability. **(C)** Western blot analysis showing a dose-dependent reduction in ZMYND8 protein levels after HMN-176 treatment. **(D)** RT-qPCR analysis showing that HMN-176 had no significant effect on ZMYND8 mRNA expression. **(E)** Western blot analysis showing increased PARP cleavage and reduced CDK6 protein levels following HMN-176 treatment. **(F)** Schematic illustration of the SK-N-BE(2) xenograft model and HMN-176 treatment schedule. **(G)** Representative bioluminescence images showing reduced tumor burden in HMN-176-treated mice compared with vehicle-treated controls. **(H)** Body weight changes during treatment, showing no significant difference between the vehicle and HMN-176 groups. **(I)** Representative images of tumors collected from vehicle- and HMN-176-treated mice at the experimental endpoint. **(J)** Quantification of tumor weight showing reduced tumor growth following HMN-176 treatment. **(K)** Representative H&E staining of liver and kidney tissues

showing no obvious pathological abnormalities after HMN-176 treatment. Data are presented as mean ± SD (n = 5 mice per group). Dose-response curves and IC_{50} values were determined by nonlinear regression. Other comparisons between two groups were performed using an unpaired two-tailed Student's t-test. "ns" indicates not significant; *P < 0.05, **P < 0.01, ***P < 0.001, ****P < 0.0001.

Figure 8. Zmynd8 promotes and HMN-176 suppresses murine neuroblastoma growth. (A) Schematic overview of Zmynd8 depletion in a murine neuroblastoma cell line established from an MYCN-driven transgenic mouse tumor. **(B)** Validation of Zmynd8 knockdown in murine neuroblastoma cells. **(C)** Cell proliferation analysis showing reduced proliferation after Zmynd8 depletion. **(D)** Western blot analysis showing decreased ZMYND8 protein levels following HMN-176 treatment. **(E)** Representative bright-field images showing growth inhibition of murine neuroblastoma cells following HMN-176 treatment. **(F)** Experimental scheme of the syngeneic subcutaneous neuroblastoma model established in C57BL/6 mice using luciferase-labeled murine neuroblastoma cells, followed by HMN-176 treatment. **(G)** Representative bioluminescence imaging of tumor-bearing mice in the vehicle and HMN-176 treatment groups. **(H)** Quantification of bioluminescence signals showing reduced tumor burden after HMN-176 treatment. **(I)** Body weight changes during treatment, showing no significant difference between the vehicle and HMN-176 groups. **(J)** Representative images of tumors collected from vehicle- and HMN-176-treated mice at the experimental endpoint. **(K)** Representative H&E staining of liver and kidney tissues showing no obvious pathological abnormalities after HMN-176 treatment. **(L) S**chematic model. Data are presented as mean ± SD (n = 5 mice per group). Unpaired two-tailed Student's t-test and one-way ANOVA were performed. "ns" indicates not significant; *P < 0.05, **P < 0.01, ***P < 0.001, ****P < 0.0001.

Supplementary Figure Legends

Supplementary Figure 1. Super-enhancer landscape and H3K27ac enrichment at the ZMYND8 locus in neuroblastoma. (A) Super-enhancer ranking and H3K27ac ChIP-seq profiles across additional NB cell lines, showing recurrent super-enhancer-associated enrichment at the *ZMYND8* locus and representative NB lineage-regulatory genes. **(B)** Additional genomic tracks showing H3K27ac enrichment surrounding the *ZMYND8* locus in the indicated NB cell lines.

Supplementary Figure 2. Validation of the biological effects of ZMYND8 depletion in neuroblastoma cells. (A) qRT-PCR confirmation of reduced *ZMYND8* expression following shRNA-mediated depletion. **(B)** Western blot validation of ZMYND8 knockdown using independent shRNAs in additional NB cell lines. **(C–D)** Additional cell proliferation assays demonstrating impaired NB cell growth following ZMYND8 knockdown. **(E)** Representative colony formation assays showing decreased clonogenic survival after ZMYND8 depletion. **(F)** Western blot analysis showing increased cleaved PARP following ZMYND8 knockdown, consistent with enhanced apoptosis. Unpaired two-tailed Student's t-test and one-way ANOVA were performed. "ns" indicates not significant; *P < 0.05, **P < 0.01, ***P < 0.001, ****P < 0.0001.

Supplementary Figure 3. Validation of ZMYND8 genomic binding and differential chromatin accessibility following ZMYND8 depletion. (A–B) Independent replicate analyses showing the genomic distribution of ZMYND8 CUT&Tag peaks across different genomic regions in SK-N-BE(2) cells, consistent with the results shown in Figure 6B. **(C)** ATAC-seq peaks with decreased chromatin accessibility following ZMYND8 knockdown. **(D)** ATAC-seq peaks with increased chromatin accessibility following ZMYND8 knockdown.

Supplementary Figure 4. ZMYND8 occupancy at regulatory regions of neuroblastoma-associated genes. (A) Genome browser view showing ZMYND8 CUT&Tag signal at regulatory regions near the *PHOX2B* locus. **(B)** Genome browser view showing ZMYND8 CUT&Tag signal at regulatory regions near the *NFIB* locus.

Supplementary Figure 5. Structure-based virtual screening strategy for ZMYND8. Structural characterization of ZMYND8 used for virtual screening. The crystal structure of human ZMYND8 (PDB: 4COS), encompassing residues 83–406 and containing the tandem PHD and bromodomain regions together with adjacent structural elements, was prepared for docking. Potential ligand-binding pockets were identified after protonation and structural optimization, and the indicated pocket was selected for subsequent virtual screening.

Supplementary Figure 6. Structure-Based Virtual Screening of Candidate ZMYND8-Binding Compounds.(A) Structural alignment of the ZMYND8 protein. **(B)** Prediction of small-molecule binding sites in the ZMYND8 4COS structure. **(C)** Molecular docking score analysis of candidate compounds. **(D–E)** Compound–protein interaction fingerprint analysis. **(F)** Structural diversity analysis of candidate compounds.

Supplementary Figure 7. Cellular effects of candidate ZMYND8-associated compounds in neuroblastoma cells. (A) Screening of the top 50 compounds ranked by the integrated virtual-screening score, showing that HMN-176 and PKD-IN-1 exhibited the strongest inhibitory effects on neuroblastoma cell viability. **(B)** Cell death analysis showing that HMN-176 increased neuroblastoma cell death in a dose-dependent manner. **(C)** Colony formation assay showing reduced clonogenic capacity following HMN-176 treatment. **(D)** Apoptosis analysis showing increased apoptotic cell death after HMN-176 treatment. Data are presented as mean±SD from three independent experiments. Unpaired two-tailed Student's t-test was performed. "ns" indicates not significant; *P < 0.05, **P < 0.01, ***P < 0.001, ****P < 0.0001.

Supplementary Figure 8. In vivo antitumor effects of HMN-176 in the SK-N-BE(2) xenograft model. (A) Quantification of bioluminescence imaging signals showing reduced tumor burden in HMN-176-treated mice compared with vehicle-treated controls. **(B)** Quantification of tumor volume showing significantly reduced tumor

growth in the HMN-176 treatment group. **(C)** Representative H&E staining of xenograft tumor tissues from vehicle- and HMN-176-treated mice. **(D)** Immunohistochemical analysis showing reduced ZMYND8 expression in tumors following HMN-176 treatment. Data are presented as mean±SD from three independent experiments. Unpaired two-tailed Student's t-test was performed. "ns" indicates not significant; *P < 0.05, **P < 0.01, ***P < 0.001, ****P < 0.0001.

Supplementary Material

Supplementary figures ,tables and methods.

Supplementary Table S1: RT-qPCR primers;

Supplementary Table S2: Antibodys;

Supplementary Table S3: Enhancer sequences;

Supplementary Table S4: shRNA sequence;

Supplementary Table S5: USP36 Hi-C Probe1-human.bait.sequence;

Supplementary Table S6: RNA-seq-BE2 shZMYND8 deseq2-gene;

Supplementary Table S7: BE2 shDHX33 GSEA HALLMARK Pathway gene;

Supplementary Table S8: CUT&Tag-BE2 ZMYND8 vs IgG -peakAnno;

Supplementary Table S9: ATAC-seq-shZMYND8 vs shNC DESeq2 results;

Supplementary Table S10: RNA-seq, ATAC-seq and CUT&Tag common genes;

Supplementary Table S11: Compounds that form direct interactions with the 4COS structure

Supplementary Table S12: Activity determination of a subset of the screened compounds

References

1. Matthay, K.K., Maris, J.M., Schleiermacher, G., Nakagawara, A., Mackall, C.L., Diller, L., and Weiss, W.A. (2016). Neuroblastoma. Nat Rev Dis Primers *2*, 16078. 10.1038/nrdp.2016.78.
2. Pugh, T.J., Morozova, O., Attiyeh, E.F., Asgharzadeh, S., Wei, J.S., Auclair, D., Carter, S.L., Cibulskis, K., Hanna, M., Kiezun, A., et al. (2013). The genetic landscape of high-risk neuroblastoma. Nat Genet *45*, 279-284. 10.1038/ng.2529.
3. Mosse, Y.P., Laudenslager, M., Longo, L., Cole, K.A., Wood, A., Attiyeh, E.F., Laquaglia, M.J., Sennett, R., Lynch, J.E., Perri, P., et al. (2008). Identification of ALK as a major familial neuroblastoma predisposition gene. Nature *455*, 930-935. 10.1038/nature07261.
4. van Groningen, T., Koster, J., Valentijn, L.J., Zwijnenburg, D.A., Akogul, N., Hasselt, N.E., Broekmans, M., Haneveld, F., Nowakowska, N.E., Bras, J., et al. (2017). Neuroblastoma is composed of two super-enhancer-associated differentiation states. Nat Genet *49*, 1261-1266. 10.1038/ng.3899.
5. Boeva, V., Louis-Brennetot, C., Peltier, A., Durand, S., Pierre-Eugene, C., Raynal, V., Etchevers, H.C., Thomas, S., Lermine, A., Daudigeos-Dubus, E., et al. (2017). Heterogeneity of neuroblastoma cell identity defined by transcriptional circuitries. Nat Genet *49*, 1408-1413. 10.1038/ng.3921.
6. Durbin, A.D., Zimmerman, M.W., Dharia, N.V., Abraham, B.J., Iniguez, A.B., Weichert-Leahey, N., He, S., Krill-Burger, J.M., Root, D.E., Vazquez, F., et al. (2018). Selective gene dependencies in MYCN-amplified neuroblastoma include the core transcriptional regulatory circuitry. Nat Genet *50*, 1240-1246. 10.1038/s41588-018-0191-z.
7. Zeid, R., Lawlor, M.A., Poon, E., Reyes, J.M., Fulciniti, M., Lopez, M.A., Scott, T.G., Nabet, B., Erb, M.A., Winter, G.E., et al. (2018). Enhancer invasion shapes MYCN-dependent transcriptional amplification in neuroblastoma. Nat Genet *50*, 515-523. 10.1038/s41588-018-0044-9.
8. Zimmerman, M.W., Liu, Y., He, S., Durbin, A.D., Abraham, B.J., Easton, J., Shao, Y., Xu, B., Zhu, S., Zhang, X., et al. (2018). MYC Drives a Subset of High-Risk Pediatric Neuroblastomas and Is Activated through Mechanisms Including Enhancer Hijacking and Focal Enhancer Amplification. Cancer Discov *8*, 320-335. 10.1158/2159-8290.CD-17-0993.
9. Qiu, B., and Matthay, K.K. (2022). Advancing therapy for neuroblastoma. Nat Rev Clin Oncol *19*, 515-533. 10.1038/s41571-022-00643-z.
10. Whyte, W.A., Orlando, D.A., Hnisz, D., Abraham, B.J., Lin, C.Y., Kagey, M.H., Rahl, P.B., Lee, T.I., and Young, R.A. (2013). Master transcription factors and mediator establish super-enhancers at key cell identity genes. Cell *153*, 307-319. 10.1016/j.cell.2013.03.035.
11. Hnisz, D., Abraham, B.J., Lee, T.I., Lau, A., Saint-Andre, V., Sigova, A.A., Hoke, H.A., and Young, R.A. (2013). Super-enhancers in the control of cell identity and disease. Cell *155*, 934-947. 10.1016/j.cell.2013.09.053.
12. Loven, J., Hoke, H.A., Lin, C.Y., Lau, A., Orlando, D.A., Vakoc, C.R., Bradner, J.E., Lee, T.I., and Young, R.A. (2013). Selective inhibition of tumor oncogenes by disruption of super-enhancers. Cell *153*, 320-334. 10.1016/j.cell.2013.03.036.
13. Oldridge, D.A., Wood, A.C., Weichert-Leahey, N., Crimmins, I., Sussman, R., Winter, C.,

McDaniel, L.D., Diamond, M., Hart, L.S., Zhu, S., et al. (2015). Genetic predisposition to neuroblastoma mediated by a LMO1 super-enhancer polymorphism. Nature *528*, 418-421. 10.1038/nature15540.

14. Chen, Y.L., Li, X.L., Li, G., Tao, Y.F., Zhuo, R., Cao, H.B., Jiao, W.Y., Li, Z.H., Zhu, Z.H., Fang, F., et al. (2022). BRD4 inhibitor GNE987 exerts anti-cancer effects by targeting super-enhancers in neuroblastoma. Cell Biosci *12*, 33. 10.1186/s13578-022-00769-8.
15. Chen, Y., Zhuo, R., Sun, L., Tao, Y., Li, G., Zhu, F., Xu, Y., Wang, J., Li, Z., Yu, J., et al. (2024). Super-enhancer-driven IRF2BP2 enhances ALK activity and promotes neuroblastoma cell proliferation. Neuro Oncol *26*, 1878-1894. 10.1093/neuonc/noae109.
16. Jia, S.Q., Zhuo, R., Zhang, Z.M., Yang, Y., Tao, Y.F., Wang, J.W., Li, X.L., Xie, Y., Li, G., Wu, D., et al. (2022). The BRD4 Inhibitor dBET57 Exerts Anticancer Effects by Targeting Superenhancer-Related Genes in Neuroblastoma. J Immunol Res *2022*, 7945884. 10.1155/2022/7945884.
17. Savitsky, P., Krojer, T., Fujisawa, T., Lambert, J.P., Picaud, S., Wang, C.Y., Shanle, E.K., Krajewski, K., Friedrichsen, H., Kanapin, A., et al. (2016). Multivalent Histone and DNA Engagement by a PHD/BRD/PWWP Triple Reader Cassette Recruits ZMYND8 to K14ac-Rich Chromatin. Cell Rep *17*, 2724-2737. 10.1016/j.celrep.2016.11.014.
18. Spruijt, C.G., Luijsterburg, M.S., Menafra, R., Lindeboom, R.G., Jansen, P.W., Edupuganti, R.R., Baltissen, M.P., Wiegant, W.W., Voelker-Albert, M.C., Matarese, F., et al. (2016). ZMYND8 Co-localizes with NuRD on Target Genes and Regulates Poly(ADP-Ribose)-Dependent Recruitment of GATAD2A/NuRD to Sites of DNA Damage. Cell Rep *17*, 783-798. 10.1016/j.celrep.2016.09.037.
19. Ghosh, K., Tang, M., Kumari, N., Nandy, A., Basu, S., Mall, D.P., Rai, K., and Biswas, D. (2018). Positive Regulation of Transcription by Human ZMYND8 through Its Association with P-TEFb Complex. Cell Rep *24*, 2141-2154 e2146. 10.1016/j.celrep.2018.07.064.
20. Servant, N., Varoquaux, N., Lajoie, B.R., Viara, E., Chen, C.J., Vert, J.P., Heard, E., Dekker, J., and Barillot, E. (2015). HiC-Pro: an optimized and flexible pipeline for Hi-C data processing. Genome Biol *16*, 259. 10.1186/s13059-015-0831-x.
21. Lareau, C.A., and Aryee, M.J. (2018). hichipper: a preprocessing pipeline for calling DNA loops from HiChIP data. Nat Methods *15*, 155-156. 10.1038/nmeth.4583.
22. Gartlgruber, M., Sharma, A.K., Quintero, A., Dreidax, D., Jansky, S., Park, Y.G., Kreth, S., Meder, J., Doncevic, D., Saary, P., et al. (2021). Super enhancers define regulatory subtypes and cell identity in neuroblastoma. Nat Cancer *2*, 114-128. 10.1038/s43018-020-00145-w.
23. Decaesteker, B., Denecker, G., Van Neste, C., Dolman, E.M., Van Loocke, W., Gartlgruber, M., Nunes, C., De Vloed, F., Depuydt, P., Verboom, K., et al. (2018). TBX2 is a neuroblastoma core regulatory circuitry component enhancing MYCN/FOXM1 reactivation of DREAM targets. Nat Commun *9*, 4866. 10.1038/s41467-018-06699-9.
24. Wang, L., Tan, T.K., Durbin, A.D., Zimmerman, M.W., Abraham, B.J., Tan, S.H., Ngoc, P.C.T., Weichert-Leahey, N., Akahane, K., Lawton, L.N., et al. (2019). ASCL1 is a MYCN- and LMO1-dependent member of the adrenergic neuroblastoma core regulatory circuitry. Nat Commun *10*, 5622. 10.1038/s41467-019-13515-5.
25. van Groningen, T., Akogul, N., Westerhout, E.M., Chan, A., Hasselt, N.E., Zwijnenburg, D.A., Broekmans, M., Stroeken, P., Haneveld, F., Hooijer, G.K.J., et al. (2019). A NOTCH feed-forward loop drives reprogramming from adrenergic to mesenchymal state in

neuroblastoma. Nat Commun *10*, 1530. 10.1038/s41467-019-09470-w.

26. Thirant, C., Peltier, A., Durand, S., Kramdi, A., Louis-Brennetot, C., Pierre-Eugene, C., Gautier, M., Costa, A., Grelier, A., Zaidi, S., et al. (2023). Reversible transitions between noradrenergic and mesenchymal tumor identities define cell plasticity in neuroblastoma. Nat Commun *14*, 2575. 10.1038/s41467-023-38239-5.
27. Henssen, A., Althoff, K., Odersky, A., Beckers, A., Koche, R., Speleman, F., Schafers, S., Bell, E., Nortmeyer, M., Westermann, F., et al. (2016). Targeting MYCN-Driven Transcription By BET-Bromodomain Inhibition. Clin Cancer Res *22*, 2470-2481. 10.1158/1078-0432.CCR-15-1449.
28. Lee, S., Rellinger, E.J., Kim, K.W., Craig, B.T., Romain, C.V., Qiao, J., and Chung, D.H. (2015). Bromodomain and extraterminal inhibition blocks tumor progression and promotes differentiation in neuroblastoma. Surgery *158*, 819-826. 10.1016/j.surg.2015.04.017.
29. Sengupta, S., and George, R.E. (2017). Super-Enhancer-Driven Transcriptional Dependencies in Cancer. Trends Cancer *3*, 269-281. 10.1016/j.trecan.2017.03.006.
30. Gong, F., Chiu, L.Y., Cox, B., Aymard, F., Clouaire, T., Leung, J.W., Cammarata, M., Perez, M., Agarwal, P., Brodbelt, J.S., et al. (2015). Screen identifies bromodomain protein ZMYND8 in chromatin recognition of transcription-associated DNA damage that promotes homologous recombination. Genes Dev *29*, 197-211. 10.1101/gad.252189.114.
31. Gong, F., Clouaire, T., Aguirrebengoa, M., Legube, G., and Miller, K.M. (2017). Histone demethylase KDM5A regulates the ZMYND8-NuRD chromatin remodeler to promote DNA repair. J Cell Biol *216*, 1959-1974. 10.1083/jcb.201611135.
32. Chen, Y., Zhang, B., Bao, L., Jin, L., Yang, M., Peng, Y., Kumar, A., Wang, J.E., Wang, C., Zou, X., et al. (2018). ZMYND8 acetylation mediates HIF-dependent breast cancer progression and metastasis. J Clin Invest *128*, 1937-1955. 10.1172/JCI95089.
33. Chen, Y., Wang, Y., and Luo, W. (2018). ZMYND8 is a primary HIF coactivator that mediates breast cancer progression. Mol Cell Oncol *5*, e1479619. 10.1080/23723556.2018.1479619.
34. Tang, B., Sun, R., Wang, D., Sheng, H., Wei, T., Wang, L., Zhang, J., Ho, T.H., Yang, L., Wei, Q., and Huang, H. (2021). ZMYND8 preferentially binds phosphorylated EZH2 to promote a PRC2-dependent to -independent function switch in hypoxia-inducible factor-activated cancer. Proc Natl Acad Sci U S A *118*. 10.1073/pnas.2019052118.
35. Luo, M., Bao, L., Chen, Y., Xue, Y., Wang, Y., Zhang, B., Wang, C., Corley, C.D., McDonald, J.G., Kumar, A., et al. (2022). ZMYND8 is a master regulator of 27-hydroxycholesterol that promotes tumorigenicity of breast cancer stem cells. Sci Adv *8*, eabn5295. 10.1126/sciadv.abn5295.
36. Carney, S.V., Banerjee, K., Mujeeb, A., Zhu, B., Haase, S., Varela, M.L., Kadiyala, P., Tronrud, C.E., Zhu, Z., Mukherji, D., et al. (2023). Zinc Finger MYND-Type Containing 8 (ZMYND8) Is Epigenetically Regulated in Mutant Isocitrate Dehydrogenase 1 (IDH1) Glioma to Promote Radioresistance. Clin Cancer Res *29*, 1763-1782. 10.1158/1078-0432.CCR-22-1896.
37. Molenaar, J.J., Ebus, M.E., Koster, J., van Sluis, P., van Noesel, C.J., Versteeg, R., and Caron, H.N. (2008). Cyclin D1 and CDK4 activity contribute to the undifferentiated phenotype in neuroblastoma. Cancer Res *68*, 2599-2609. 10.1158/0008-5472.CAN-07-5032.

38. Rader, J., Russell, M.R., Hart, L.S., Nakazawa, M.S., Belcastro, L.T., Martinez, D., Li, Y., Carpenter, E.L., Attiyeh, E.F., Diskin, S.J., et al. (2013). Dual CDK4/CDK6 inhibition induces cell-cycle arrest and senescence in neuroblastoma. Clin Cancer Res *19*, 6173-6182. 10.1158/1078-0432.CCR-13-1675.

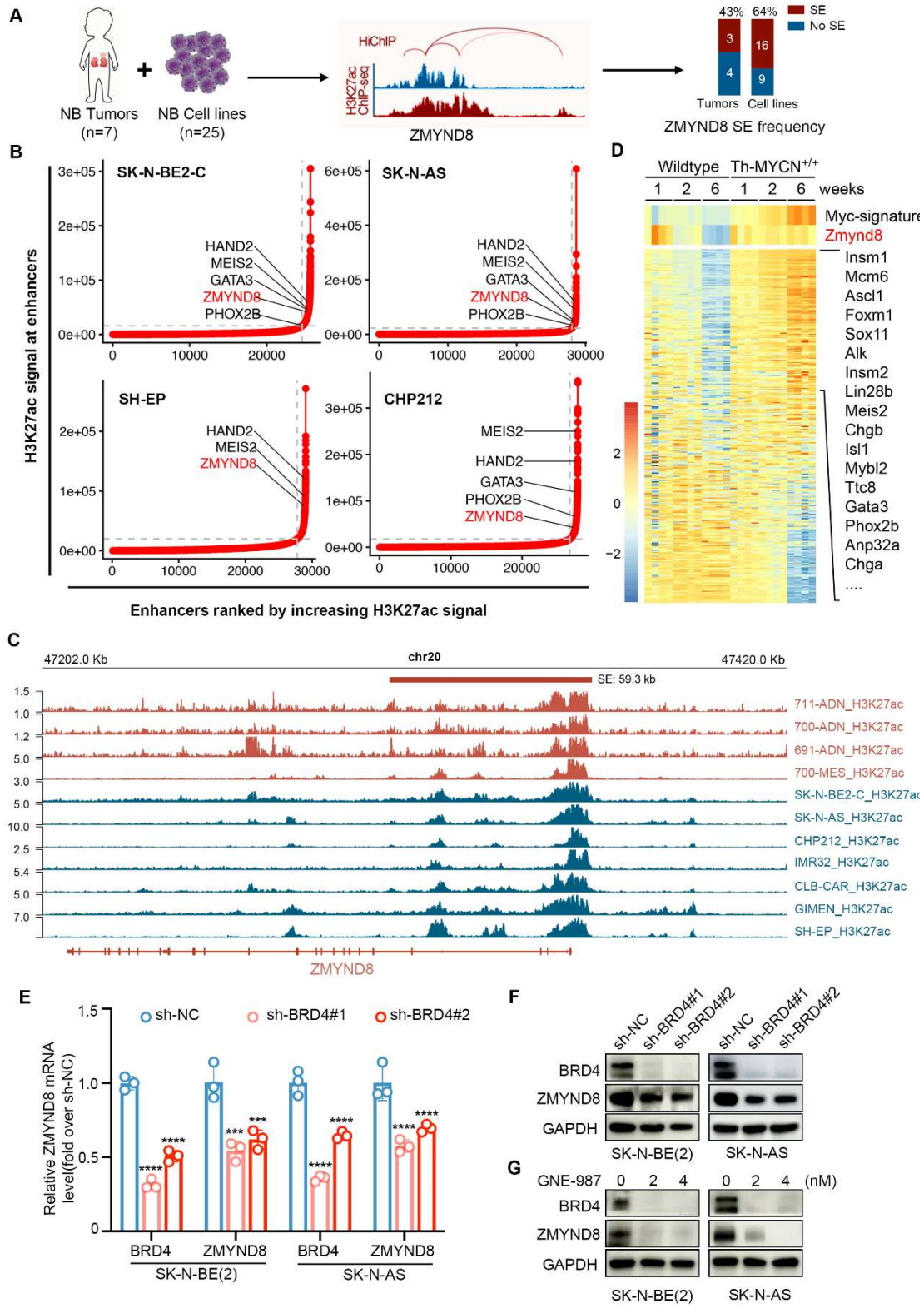
39. Rihani, A., Vandesompele, J., Speleman, F., and Van Maerken, T. (2015). Inhibition of CDK4/6 as a novel therapeutic option for neuroblastoma. Cancer Cell Int *15*, 76. 10.1186/s12935-015-0224-y.

40. Ferguson, K.M., Gillen, S.L., Chaytor, L., Poon, E., Marcos, D., Gomez, R.L., Woods, L.M., Mykhaylechko, L., Elfari, L., Martins da Costa, B., et al. (2023). Palbociclib releases the latent differentiation capacity of neuroblastoma cells. Dev Cell *58*, 1967-1982 e1968. 10.1016/j.devcel.2023.08.028.

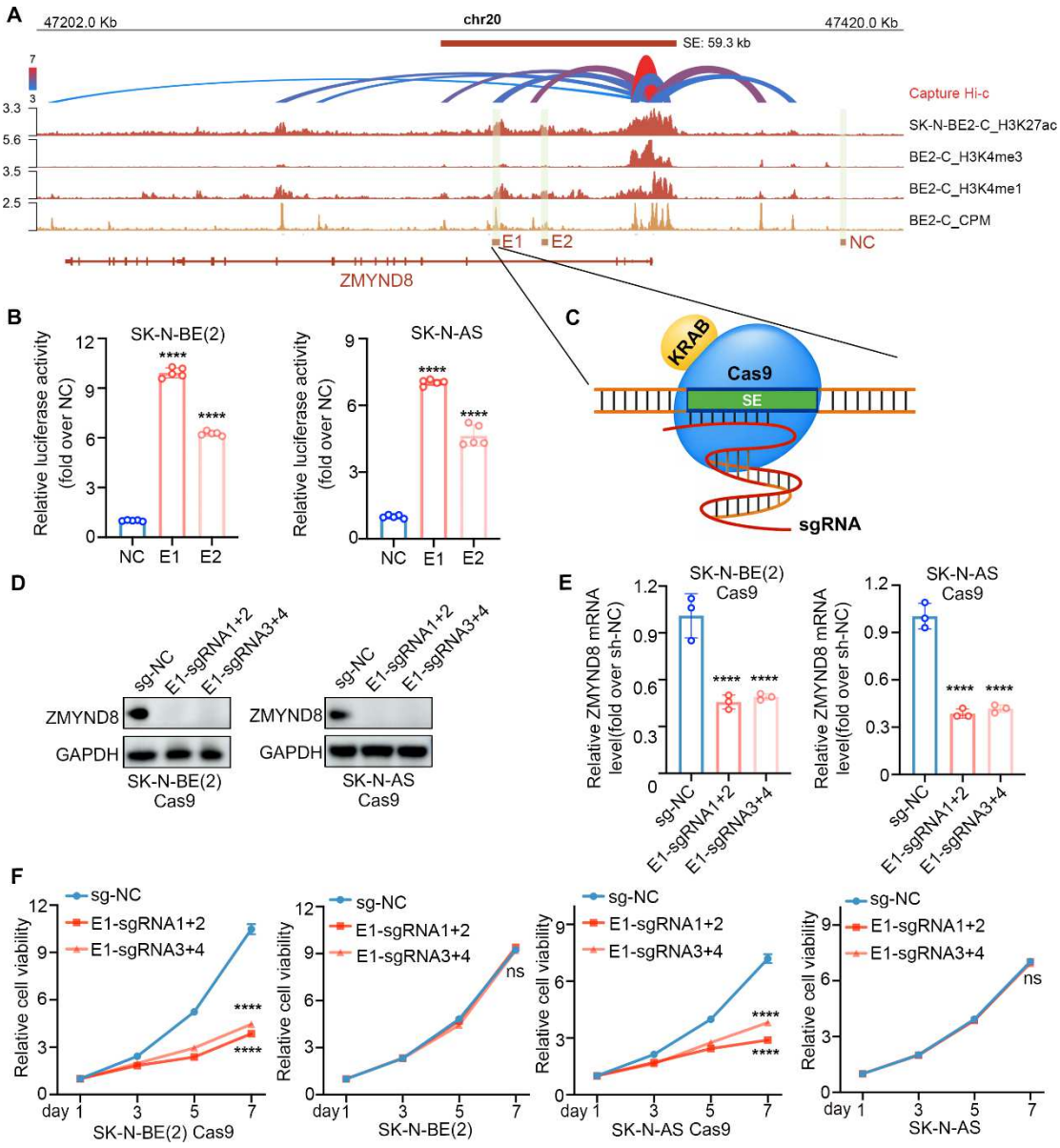
41. Tanaka, H., Ohshima, N., Ikenoya, M., Komori, K., Katoh, F., and Hidaka, H. (2003). HMN-176, an active metabolite of the synthetic antitumor agent HMN-214, restores chemosensitivity to multidrug-resistant cells by targeting the transcription factor NF-Y. Cancer Res *63*, 6942-6947.

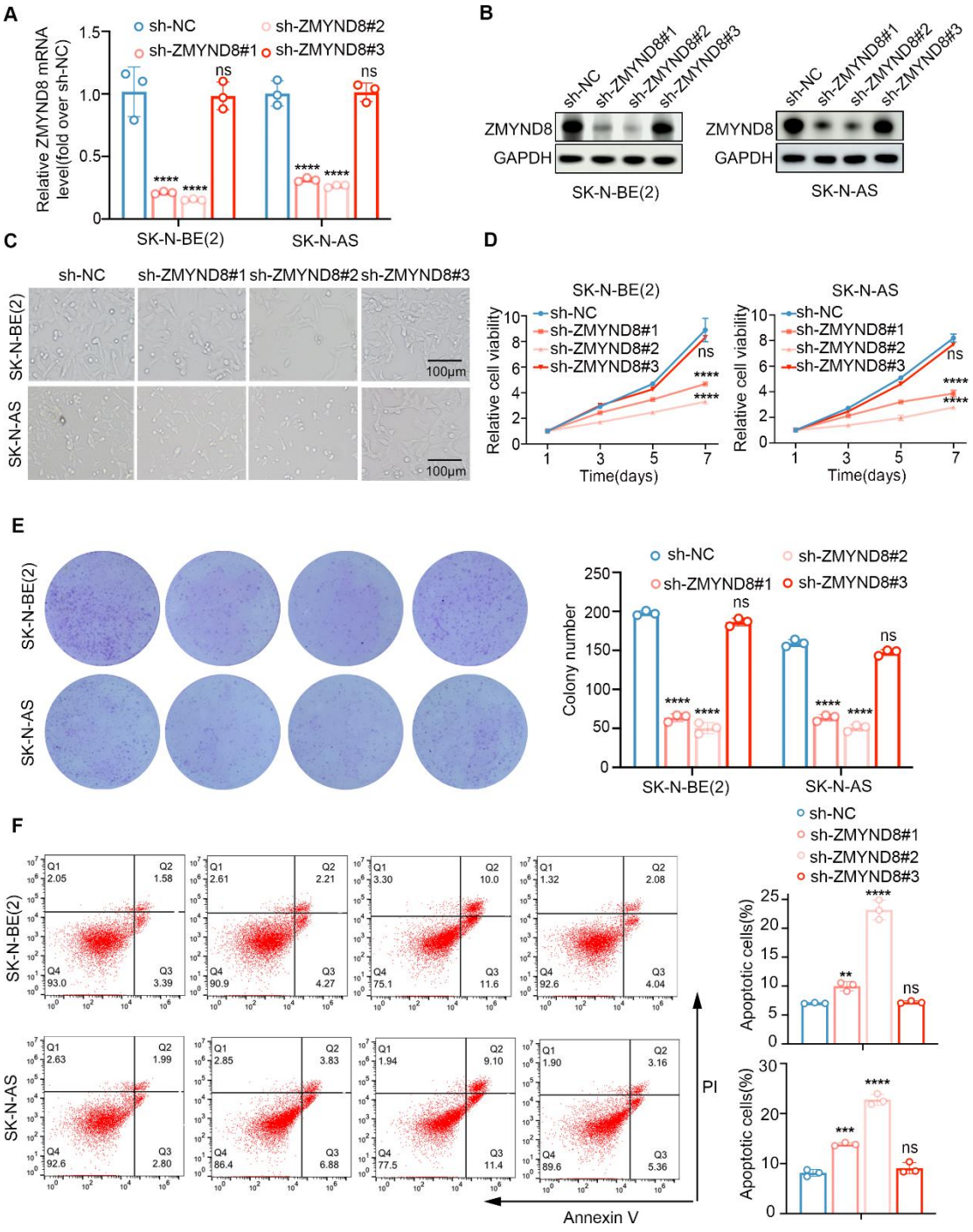
42. DiMaio, M.A., Mikhailov, A., Rieder, C.L., Von Hoff, D.D., and Palazzo, R.E. (2009). The small organic compound HMN-176 delays satisfaction of the spindle assembly checkpoint by inhibiting centrosome-dependent microtubule nucleation. Mol Cancer Ther *8*, 592-601. 10.1158/1535-7163.MCT-08-0876.

43. Chilamakuri, R., Rouse, D.C., and Agarwal, S. (2022). Inhibition of Polo-like Kinase 1 by HMN-214 Blocks Cell Cycle Progression and Inhibits Neuroblastoma Growth. Pharmaceuticals (Basel) *15*. 10.3390/ph15050523.

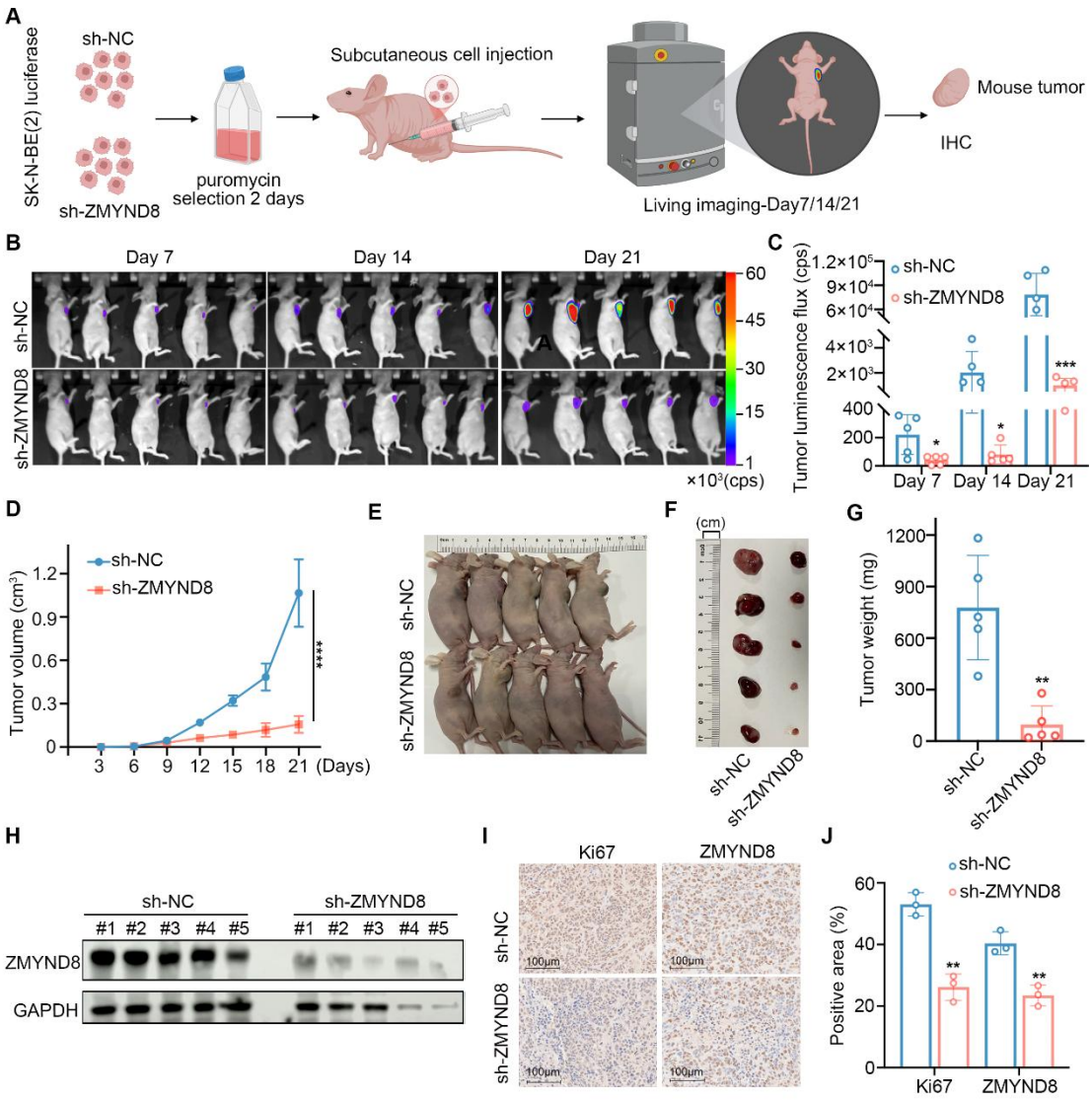

A
NB Tumors (n=7)
NB Cell lines (n=25)
HiChIP
H3K27ac ChIP-seq
ZMYND8
43%
64%
SE
No SE
3
16
4
9
Tumors
Cell lines
ZMYND8 SE frequency
B
SK-N-BE2-C
SK-N-AS
SH-EP
CHP212
HAND2
MEIS2
GATA3
ZMYND8
PHOX2B
H3K27ac signal at enhancers
Enhancers ranked by increasing H3K27ac signal
C
47202.0 Kb
chr20
47420.0 Kb
SE: 59.3 kb
711-ADN_H3K27ac
700-ADN_H3K27ac
691-ADN_H3K27ac
700-MES_H3K27ac
SK-N-BE2-C_H3K27ac
SK-N-AS_H3K27ac
CHP212_H3K27ac
IMR32_H3K27ac
CLB-CAR_H3K27ac
GIMEN_H3K27ac
SH-EP_H3K27ac
ZMYND8
D
Wildtype
Th-MYCN+/+
1 2 6 1 2 6 weeks
Myc-signature
Zmynd8
Insm1
Mcm6
Ascl1
Foxm1
Sox11
Alk
Insm2
Lin28b
Meis2
Chgb
Isl1
Mybl2
Ttc8
Gata3
Phox2b
Anp32a
Chga
....
E
sh-NC
sh-BRD4#1
sh-BRD4#2
Relative ZMYND8 mRNA level(fold over sh-NC)
BRD4
ZMYND8
SK-N-BE(2)
SK-N-AS
F
sh-NC
sh-BRD4#1
sh-BRD4#2
BRD4
ZMYND8
GAPDH
SK-N-BE(2)
SK-N-AS
G
GNE-987 0 2 4 0 2 4 (nM)
BRD4
ZMYND8
GAPDH
SK-N-BE(2)
SK-N-AS

1

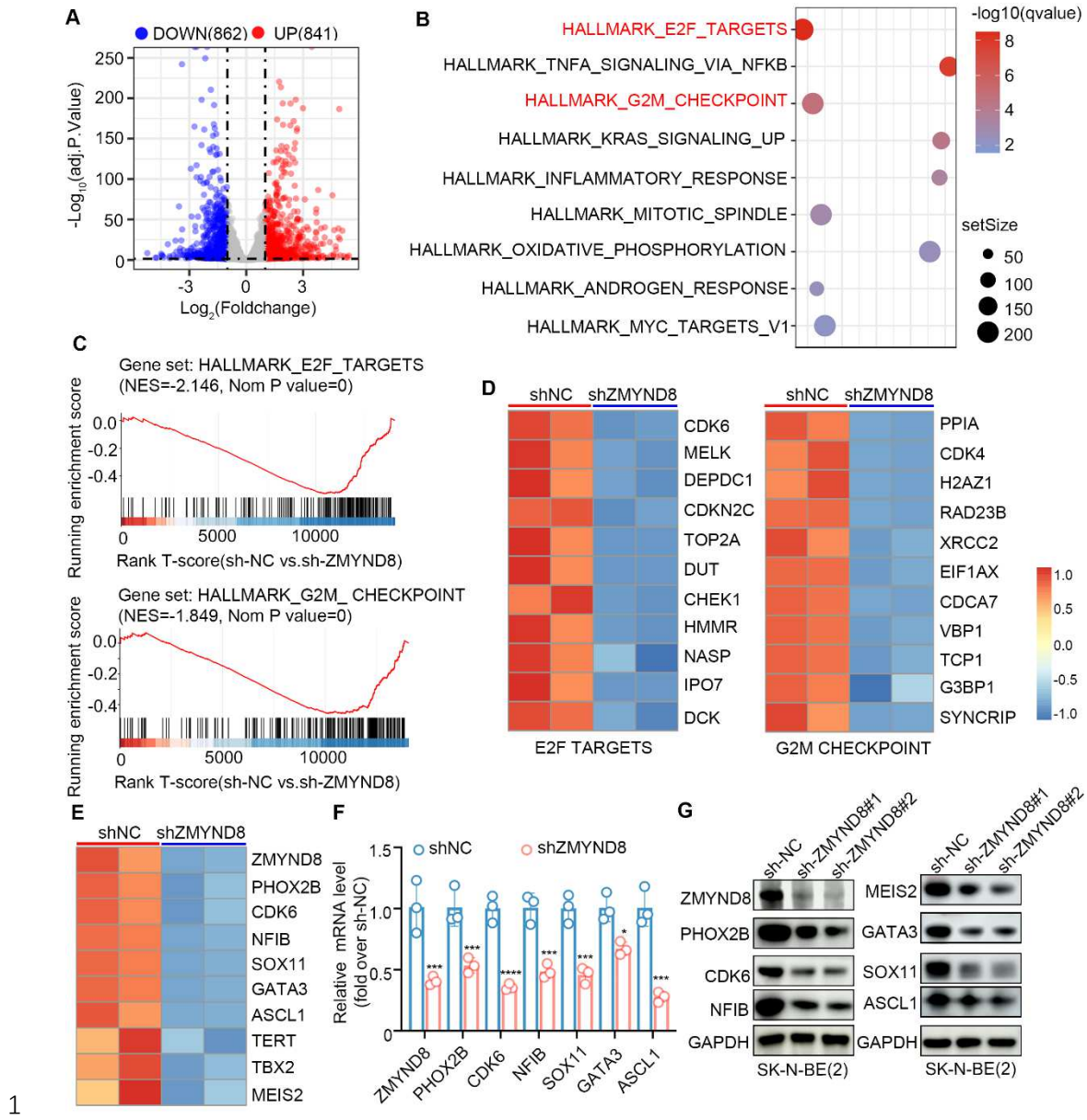

A
47202.0 Kb
chr20
47420.0 Kb
SE: 59.3 kb
Capture Hi-c
SK-N-BE2-C_H3K27ac
BE2-C_H3K4me3
BE2-C_H3K4me1
BE2-C_CPM
E1
E2
NC
ZMYND8
B
SK-N-BE(2)
SK-N-AS
Relative luciferase activity (fold over NC)
NC
E1
E2
C
KRAB
Cas9
SE
sgRNA
D
sg-NC
E1-sgRNA1+2
E1-sgRNA3+4
ZMYND8
GAPDH
SK-N-BE(2) Cas9
SK-N-AS Cas9
E
Relative ZMYND8 mRNA level(fold over sh-NC)
F
Relative cell viability
day
ns


A
Relative ZMYND8 mRNA level(fold over sh-NC)
sh-NC
sh-ZMYND8#1
sh-ZMYND8#2
sh-ZMYND8#3
ns
****
SK-N-BE(2)
SK-N-AS
B
ZMYND8
GAPDH
SK-N-BE(2)
SK-N-AS
C
sh-NC
sh-ZMYND8#1
sh-ZMYND8#2
sh-ZMYND8#3
SK-N-BE(2)
SK-N-AS
100μm
D
SK-N-BE(2)
SK-N-AS
Relative cell viability
Time(days)
E
SK-N-BE(2)
SK-N-AS
Colony number
F
SK-N-BE(2)
SK-N-AS
PI
Annexin V
Apoptotic cells(%)

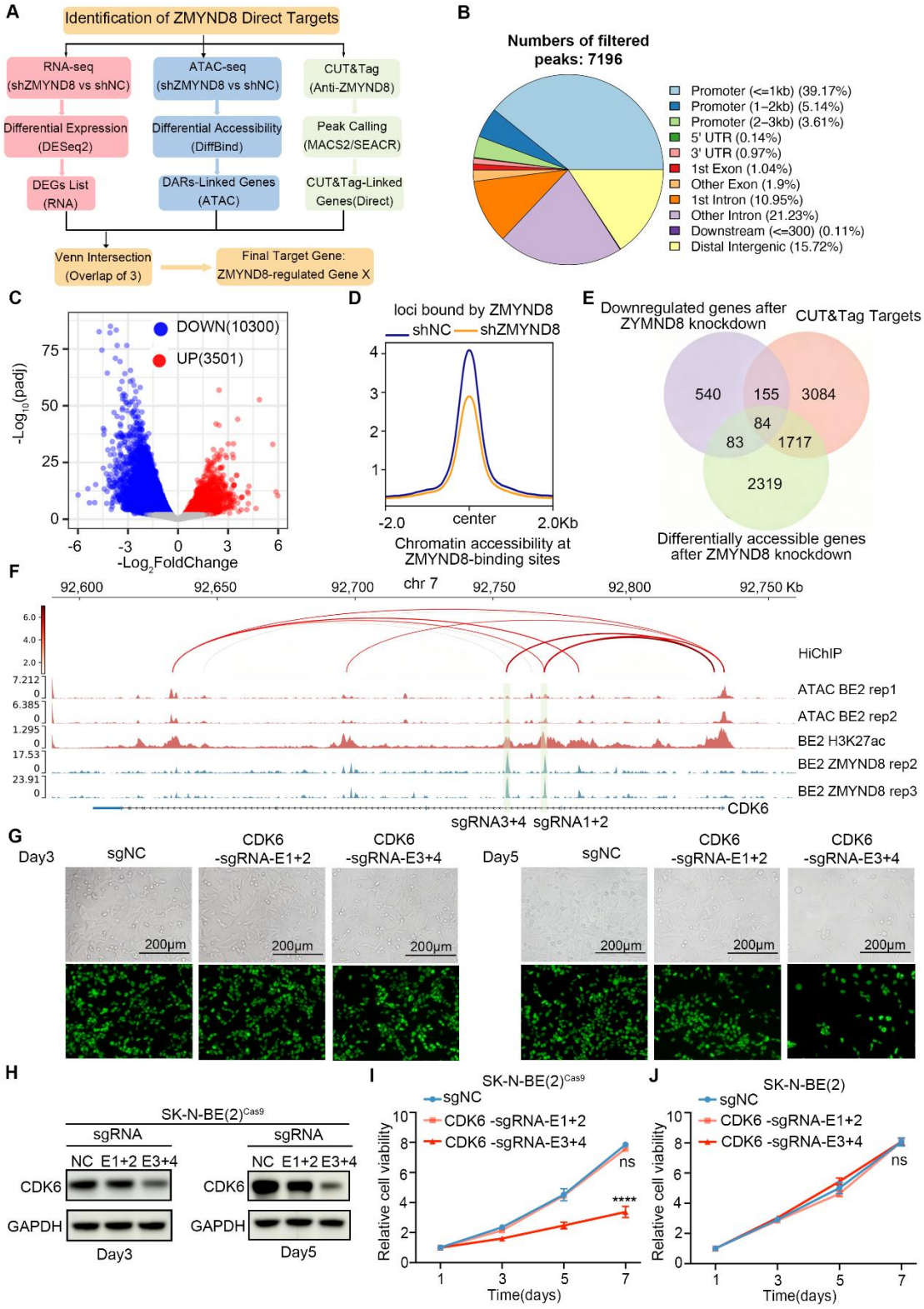
1


A
SK-N-BE(2) luciferase
sh-NC
sh-ZMYND8
puromycin selection 2 days
Subcutaneous cell injection
Living imaging-Day7/14/21
Mouse tumor
IHC
B
Day 7
Day 14
Day 21
sh-NC
sh-ZMYND8
×10³(cps)
C
Tumor luminescence flux (cps)
sh-NC
sh-ZMYND8
Day 7 Day 14 Day 21
D
Tumor volume (cm³)
sh-NC
sh-ZMYND8
(Days)
E
F
(cm)
G
Tumor weight (mg)
H
sh-NC
sh-ZMYND8
ZMYND8
GAPDH
I
Ki67
ZMYND8
J
Positive area (%)
Ki67
ZMYND8

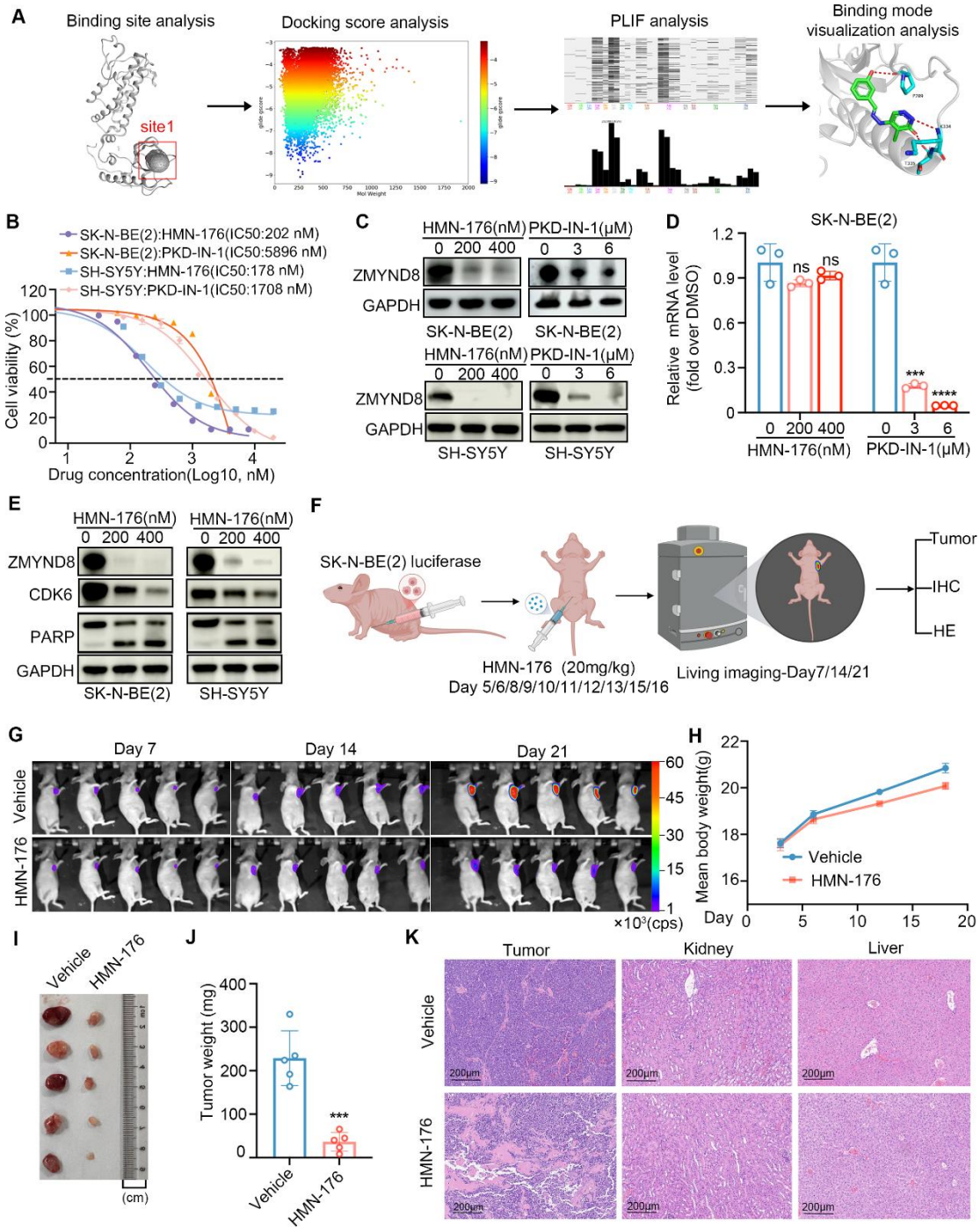
1


A
DOWN(862)
UP(841)
-Log10(adj.P.Value)
Log2(Foldchange)
B
HALLMARK_E2F_TARGETS
HALLMARK_TNFA_SIGNALING_VIA_NFKB
HALLMARK_G2M_CHECKPOINT
HALLMARK_KRAS_SIGNALING_UP
HALLMARK_INFLAMMATORY_RESPONSE
HALLMARK_MITOTIC_SPINDLE
HALLMARK_OXIDATIVE_PHOSPHORYLATION
HALLMARK_ANDROGEN_RESPONSE
HALLMARK_MYC_TARGETS_V1
-log10(qvalue)
setSize
C
Gene set: HALLMARK_E2F_TARGETS
(NES=-2.146, Nom P value=0)
Running enrichment score
Rank T-score(sh-NC vs.sh-ZMYND8)
Gene set: HALLMARK_G2M_ CHECKPOINT
(NES=-1.849, Nom P value=0)
D
shNC
shZMYND8
CDK6
MELK
DEPDC1
CDKN2C
TOP2A
DUT
CHEK1
HMMR
NASP
IPO7
DCK
E2F TARGETS
PPIA
CDK4
H2AZ1
RAD23B
XRCC2
EIF1AX
CDCA7
VBP1
TCP1
G3BP1
SYNCRIP
G2M CHECKPOINT
E
ZMYND8
PHOX2B
CDK6
NFIB
SOX11
GATA3
ASCL1
TERT
TBX2
MEIS2
F
Relative mRNA level
(fold over sh-NC)
G
sh-NC
sh-ZMYND8#1
sh-ZMYND8#2
GAPDH
SK-N-BE(2)

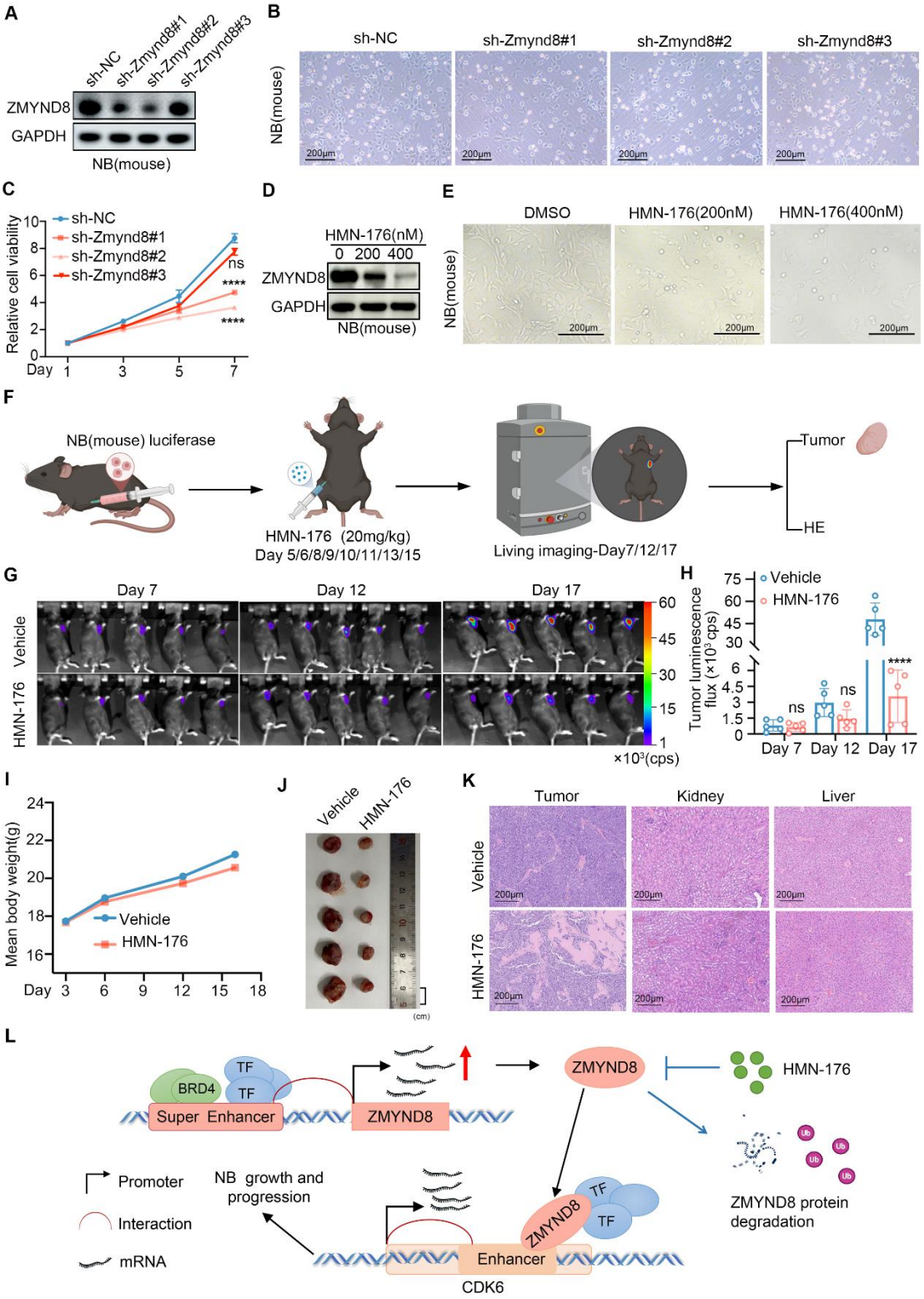
1


A
Identification of ZMYND8 Direct Targets
RNA-seq (shZMYND8 vs shNC)
ATAC-seq (shZMYND8 vs shNC)
CUT&Tag (Anti-ZMYND8)
Differential Expression (DESeq2)
Differential Accessibility (DiffBind)
Peak Calling (MACS2/SEACR)
DEGs List (RNA)
DARs-Linked Genes (ATAC)
CUT&Tag-Linked Genes(Direct)
Venn Intersection (Overlap of 3)
Final Target Gene: ZMYND8-regulated Gene X
B
Numbers of filtered peaks: 7196
Promoter (<=1kb) (39.17%)
Promoter (1–2kb) (5.14%)
Promoter (2–3kb) (3.61%)
5' UTR (0.14%)
3' UTR (0.97%)
1st Exon (1.04%)
Other Exon (1.9%)
1st Intron (10.95%)
Other Intron (21.23%)
Downstream (<=300) (0.11%)
Distal Intergenic (15.72%)
C
DOWN(10300)
UP(3501)
-Log10(padj)
-Log2FoldChange
D
loci bound by ZMYND8
shNC
shZMYND8
center
2.0Kb
Chromatin accessibility at ZMYND8-binding sites
E
Downregulated genes after ZYMND8 knockdown
CUT&Tag Targets
540
155
3084
84
83
1717
2319
Differentially accessible genes after ZMYND8 knockdown
F
92,600
92,650
92,700
chr 7
92,750
92,800
92,750 Kb
HiChIP
ATAC BE2 rep1
ATAC BE2 rep2
BE2 H3K27ac
BE2 ZMYND8 rep2
BE2 ZMYND8 rep3
CDK6
sgRNA3+4
sgRNA1+2
G
Day3
sgNC
CDK6 -sgRNA-E1+2
CDK6 -sgRNA-E3+4
Day5
200μm
H
SK-N-BE(2)Cas9
sgRNA
NC
E1+2
E3+4
CDK6
GAPDH
Day3
Day5
I
SK-N-BE(2)Cas9
sgNC
CDK6 -sgRNA-E1+2
CDK6 -sgRNA-E3+4
Relative cell viability
Time(days)
ns
****
J
SK-N-BE(2)
sgNC
CDK6 -sgRNA-E1+2
CDK6 -sgRNA-E3+4
Relative cell viability
Time(days)
ns

1


A
Binding site analysis
site1
Docking score analysis
PLIF analysis
Binding mode visualization analysis
B
SK-N-BE(2):HMN-176(IC50:202 nM)
SK-N-BE(2):PKD-IN-1(IC50:5896 nM)
SH-SY5Y:HMN-176(IC50:178 nM)
SH-SY5Y:PKD-IN-1(IC50:1708 nM)
Cell viability (%)
Drug concentration(Log10, nM)
C
HMN-176(nM) 0 200 400
PKD-IN-1(μM) 0 3 6
ZMYND8
GAPDH
SK-N-BE(2)
SH-SY5Y
D
SK-N-BE(2)
Relative mRNA level (fold over DMSO)
ns
***
****
HMN-176(nM)
PKD-IN-1(μM)
E
HMN-176(nM) 0 200 400
ZMYND8
CDK6
PARP
GAPDH
SK-N-BE(2)
SH-SY5Y
F
SK-N-BE(2) luciferase
HMN-176 (20mg/kg)
Day 5/6/8/9/10/11/12/13/15/16
Living imaging-Day7/14/21
Tumor
IHC
HE
G
Day 7
Day 14
Day 21
Vehicle
HMN-176
×10³(cps)
H
Mean body weight(g)
Day
Vehicle
HMN-176
I
Vehicle
HMN-176
(cm)
J
Tumor weight (mg)
***
Vehicle
HMN-176
K
Tumor
Kidney
Liver
Vehicle
HMN-176
200μm

1


A
sh-NC
sh-Zmynd8#1
sh-Zmynd8#2
sh-Zmynd8#3
ZMYND8
GAPDH
NB(mouse)
B
sh-NC
sh-Zmynd8#1
sh-Zmynd8#2
sh-Zmynd8#3
NB(mouse)
200μm
C
Relative cell viability
sh-NC
sh-Zmynd8#1
sh-Zmynd8#2
sh-Zmynd8#3
ns
****
****
Day
D
HMN-176(nM)
0 200 400
ZMYND8
GAPDH
NB(mouse)
E
DMSO
HMN-176(200nM)
HMN-176(400nM)
NB(mouse)
200μm
F
NB(mouse) luciferase
HMN-176 (20mg/kg)
Day 5/6/8/9/10/11/13/15
Living imaging-Day7/12/17
Tumor
HE
G
Day 7
Day 12
Day 17
Vehicle
HMN-176
×10³(cps)
H
Vehicle
HMN-176
Tumor luminescence flux (×10³ cps)
ns
ns
****
Day 7
Day 12
Day 17
I
Mean body weight(g)
Vehicle
HMN-176
Day
J
Vehicle
HMN-176
(cm)
K
Tumor
Kidney
Liver
Vehicle
HMN-176
200μm
L
BRD4
TF
TF
Super Enhancer
ZMYND8
ZMYND8
HMN-176
Promoter
Interaction
mRNA
NB growth and progression
ZMYND8
TF
TF
Enhancer
CDK6
Ub
ZMYND8 protein degradation

1

Supplementary Files

This is a list of supplementary files associated with this preprint. Click to download.

- SupplementaryTableS1.xlsx
- SupplementaryTableS5.xlsx
- SupplementaryTableS7.xls
- SupplementaryTableS10.csv
- SupplementaryTableS8.csv
- SupplementaryTableS11.xls
- SupplementaryTableS2.xlsx
- SupplementaryTableS6.csv
- SupplementaryTableS3.xlsx
- SupplementaryTableS9.csv
- Originalblot.pdf
- SupplementaryFigures.pdf
- Supplementarymethods.docx
- SupplementaryTableS4.xlsx
- SupplementaryTableS12.xlsx